

© 2025 IEEE. Personal use of this material is permitted. Permission from IEEE must be obtained for all other uses, including reprinting/republishing this material for advertising or promotional purposes, collecting new collected works for resale or redistribution to servers or lists, or reuse of any copyrighted component of this work in other works. This work has been submitted to the IEEE for possible publication. Copyright may be transferred without notice, after which this version may no longer be accessible.

Surrogate-Enhanced Modeling and Adaptive Modular Control of All-Electric Heavy-Duty Robotic Manipulators

Amir Hossein Barjini, Mohammad Bahari, Mahdi Hejrati, and Jouni Mattila

Abstract—This paper presents a unified system-level modeling and control framework for an all-electric heavy-duty robotic manipulator (HDRM) driven by electromechanical linear actuators (EMLAs). A surrogate-enhanced actuator model, combining integrated electromechanical dynamics with a neural network trained on a dedicated testbed, is integrated into an extended virtual decomposition control (VDC) architecture augmented by a natural adaptation law. The derived analytical HDRM model supports a hierarchical control structure that seamlessly maps high-level force and velocity objectives to real-time actuator commands, accompanied by a Lyapunov-based stability proof. In multi-domain simulations of both cubic and a custom planar triangular trajectories, the proposed adaptive modular controller achieves sub-centimeter Cartesian tracking accuracy. Experimental validation of the same 1-DoF platform under realistic load emulation confirms the efficacy of the proposed control strategy. These findings demonstrate that a surrogate-enhanced EMLA model embedded in the VDC approach can enable modular, real-time control of an all-electric HDRM, supporting its deployment in next-generation mobile working machines.

Note to Practitioners—Modern mobile working machines increasingly demand fully electric actuation to meet stringent efficiency, emissions, and maintenance targets. This paper presents a modeling and control framework for all-electric heavy-duty manipulators driven by electromechanical linear actuators (EMLAs). We begin by integrating first-principles electromechanical dynamics with a deep neural-network surrogate trained on real actuator data, capturing unmodeled friction, compliance, and losses without sacrificing interpretability or real-time performance. Next, we embed this hybrid actuator model into an extended virtual decomposition control architecture, which is a decentralized, hierarchical controller featuring a Lyapunov-based natural adaptation law that guarantees stability and robustness to $\pm 40\%$ parameter variations. In multi-domain simulations on cubic and custom triangular trajectories, the controller achieves sub-centimeter accuracy (under 2 mm Cartesian RMSE), and hardware experiments on a 1-DoF testbed under dynamic load emulation confirm this level of performance. Practitioners can leverage this modular framework to retrofit existing machine architectures with EMLAs or to design next-generation electric manipulators, benefiting from precise motion control.

Index Terms—Adaptive Modular Control, Electromechanical Linear Actuator, Heavy-Duty Robotic Manipulator, Deep Neural Network, Surrogate-Enhanced Modeling, Virtual Decomposition Control

I. INTRODUCTION

Funding for this research was provided by the Business Finland partnership project “Future All-Electric Rough Terrain Autonomous Mobile Manipulators” (Grant No. 2334/31/2022).

All authors are with the Department of Engineering and Natural Sciences, Tampere University, 7320 Tampere, Finland (e-mails: amirhossein.barjini@tuni.fi, mohammad.bahari@tuni.fi, mahdi.hejrati@tuni.fi, jouni.mattila@tuni.fi).

ROBOT manipulation plays a crucial role across a broad range of applications, encompassing both mobile systems [1] and stationary manipulators [2], [3], popular examples of which are heavy-duty robotic manipulators (HDRMs), utilized in such industrial sectors as off-road machinery, construction, agriculture, and forestry [4]. However, significant challenges to achieving dexterous and adaptable manipulation capabilities remain [5], particularly as the number of degrees of freedom (DOF) increases, HDRM control becomes increasingly complex [6].

A. Controlling Heavy-Duty Robotic Manipulators

To address the complex challenges associated with controlling HDRMs, a range of advanced strategies has been explored in recent studies. For instance, adaptive robust control techniques [7] aim to compensate for modeling uncertainties and external disturbances, while nonlinear model predictive control (NMPC) [8] enables optimal trajectory tracking under system constraints. Further, adaptive neural network-based control [9] leverages learning capabilities to handle nonlinearities and time-varying dynamics, and data-driven reinforcement learning approaches [10] have emerged as promising tools for developing control policies through direct interaction with the environment, without requiring an explicit model. In addition, hybrid control approaches that combine backstepping, sliding mode, and neural network techniques have also been proposed to manage complex nonlinearities and completely unknown system dynamics in electro-hydraulic actuators [11]. Meanwhile, another widely adopted method is virtual decomposition control (VDC), a modular and model-based control approach [12] that, due to its structured design and performance, has attracted considerable attention in recent years and has been widely applied to the motion control of HDRMs [13]–[17]. A comparative analysis also demonstrated that VDC achieves an acceptable tracking error at higher speeds [14].

With the increasing adoption of electrified actuation systems, considerable attention has been directed toward developing control strategies specifically suited for electric manipulators driven by permanent magnet synchronous motors (PMSMs). Adaptive neural sliding mode control approaches have thus been introduced to enhance speed regulation and robustness against dynamic uncertainties in PMSM systems [18]. In addition, model-free and observer-based sliding mode control techniques have been proposed to address the limitations of model dependency by estimating unmodeled dynamics and external disturbances through robust observers [19]. Robust model predictive control (MPC) has also been applied to three-phase PMSM drives, demonstrating improved performance in

terms of current tracking accuracy and resilience to parameter variations [20]. In effect, these advancements underscore the growing maturity of control solutions tailored for electrically actuated manipulators.

B. Electrification of Heavy-Duty Robotic Manipulators

The escalating urgency of the climate crisis, alongside a growing international consensus on the need for carbon neutrality, has significantly accelerated the shift toward electrified systems across both the transportation and off-highway machinery sectors [21]–[23]. Regulatory frameworks, such as the Paris Agreement [24], the European Union (EU)’s proposed 2035 ban on internal combustion engine (ICE) vehicles [25], and Advanced Motor Fuels (AMF) Annex 50 [26] have set ambitious targets for reducing emissions, thereby encouraging the development of low-emission powertrains and electric actuation systems in mobile working machines (MWMs) [27], [28]. In response to the broader push toward electrification, both industry and academia have increasingly focused on developing modular, battery-compatible mechanisms that support scalable deployment across various classes of MWMs. One representative category is vehicle-mounted lifting and manipulation mechanisms, including loader cranes, tail lifts, and articulated booms, which occupy a transitional space between conventional MWMs and fully coordinated HDRMs [29].

Traditionally powered by hydraulic linear actuators (HLAs), these systems offer a valuable platform for evaluating the integration of electromechanical linear actuators (EMLAs) under realistic load and duty-cycle conditions [30]. Through such intermediate applications, researchers have shown that electromechanical-based architectures improve energy efficiency and enable regenerative energy recovery [31], and these findings provide a practical foundation for extending EMLA adoption into HDRMs, where minimizing total energy consumption and maximizing battery life are essential to the viability of fully electric systems [32]. The replacement of HLAs with EMLAs, which are typically driven by PMSMs and integrated with high-efficiency roller-screw mechanisms, enables precise [33], high-response [34], smooth [35], and clean actuation [36]. In addition, EMLAs also support direct electrical control of linear motion, enhanced fault detection and isolation, and predictable performance under varying load conditions [37], [38], with recent advances in position sensing having further enabled the high-precision feedback needed for PMSMs of EMLA [39]–[41].

Notably, by demonstrating the feasibility of all-electric actuation in real-world, industrial-grade machinery, the fully electric Bobcat T7X compact track loader [42] and the Volvo EX03 mid-sized electric excavator [43] represent significant milestones, showcasing technical maturity, commercial readiness, and operational advantages in rugged, high-power applications with clean operation [44], [45]. While these achievements underscore the viability of all-electric actuation in MWMs, this also opens an opportunity to investigate how such technologies can be extended to more dynamically complex, multi-DoF HDRMs, for which integrated modeling and coordinated control are critical.

C. Motivations and Research Gap

EMLAs represent promising alternatives to traditional hydraulic systems for HDRMs, delivering clean actuation, improved energy efficiency, enhanced control precision, and significantly reduced maintenance requirements. Driven by escalating sustainability objectives and regulatory demands, the transition toward all-electric HDRMs has become increasingly essential. However, integrating EMLAs into multi-DoF manipulators poses complicated multi-domain interaction and control challenges [46]. Despite notable progress in the actuator-level modeling and control design of single-DoF EMLAs [47]–[49], extending these efforts to comprehensive all-electric HDRM assemblies with multiple interacting joints remains underexplored [50]. Therefore, ensuring effective operation and the realization of the full benefits of EMLA-driven HDRMs depends on a rigorous system-level modeling and coordinated control strategy to enable accurate motion tracking and ensure robust responsiveness to disturbances [51]–[53].

Motivated by these research gaps and the necessity to employ a scalable modeling and control strategy for all-electric HDRMs, there is a critical need for an integrated framework capable of capturing the synergistic interaction between actuator- and manipulator-level dynamics. In this context, the VDC framework, recognized for its modular and model-based formulation, provides a compelling foundation, but to the best of the authors’ knowledge, its practical applications have thus far been limited to hydraulically actuated HDRMs. Thus, extending VDC to incorporate high-fidelity, empirically validated EMLA models that ensure rigorous physical consistency, capture essential electromechanical interactions, and guarantee closed-loop stability is imperative.

D. Contributions and Structure of the Paper

This paper addresses the paradigm shift toward HDRM electrification by developing a comprehensive, high-fidelity modeling and adaptive modular control framework for an all-electric 6-DoF manipulator actuated exclusively by EMLAs. By leveraging the VDC methodology, the presented approach captures the intricate interactions between actuator- and manipulator-level dynamics, ensuring a robust performance against parametric uncertainties under realistic conditions. The proposed framework aims to contribute to the ongoing transition toward all-electric HDRMs by addressing key modeling and control challenges that have limited the deployment of fully electric manipulation systems.

The methodological framework and primary contributions of this study are summarized as follows:

- Development of a surrogate-enhanced EMLA modeling framework that integrates empirical data with physics-based actuator dynamics and that accurately captures nonlinear behaviors, energy conversion inefficiencies, and unmodeled losses to achieve a hybrid model of the actuation mechanism.
- Derivation of detailed kinematic and dynamic models of a 6-DoF manipulator using the VDC methodology, accounting for complex mechanical linkages including

three-bar and four-bar mechanisms, and enabling systematic integration with EMLA behavior.

- Formulation and implementation of a low-level controller for each EMLA-based on the surrogate-enhanced model that simultaneously regulates current, force, and velocity, ensuring stable closed-loop actuator behavior.
- Extension and embedding of this hybrid actuator model within an adaptive modular VDC architecture, enabling decentralized yet coordinated control of complex multi-domain interactions, effectively addressing both actuator- and manipulator-level control complexities.
- Lyapunov-based stability proof demonstrating that the combined rigid-body subsystems and low-level EMLA controllers yield an asymptotically stable closed-loop system.
- Comprehensive performance assessment under cubic and custom planar trajectories, highlighting precise trajectory tracking, robustness to parametric uncertainties, and consistent control performance across diverse operational scenarios.
- Rigorous validation of the proposed framework through simulations and experimental evaluations on a dedicated 1-DoF EMLA testbed. Representative joint-level motion profiles extracted from comprehensive 6-DoF manipulator simulations ensure practical feasibility and robustness.

The remainder of the paper is organized as follows. Section II presents the theoretical and mathematical foundations of the VDC framework and derives the complete electromechanical model of the EMLA mechanism, covering rigid-body kinematics and dynamics, velocity/force transformations, the natural adaptation law (NAL), stability definitions, and the actuator's dq -frame electrical and mechanical dynamics. Section III outlines the building of the unified system model: first the analytical HDRM model is presented, with a systematic kinematic chain formulation for each link and recursive force/moment dynamics under VDC; then, the surrogate-enhanced hybrid EMLA model is developed by blending model-based dynamics with data-driven corrections. In Section IV, we embed the actuator model into an adaptive modular VDC controller, derive the required joint and task-space velocities and forces, design low-level voltage and current controllers for each EMLA, and provide a Lyapunov-based stability proof. Section V evaluates system performance through cubic and custom planar trajectories, first in simulation by analyzing tracking accuracy, and then experimentally on a 1-DoF testbed. Finally, Section VI summarizes the contributions and outlines avenues for future research.

II. MATHEMATICAL FOUNDATIONS OF VDC AND THE EMLA MECHANISM

Before presenting the main contributions, this section introduces fundamental concepts related to the VDC approach and the dynamic modeling of EMLAs.

A. VDC Preliminaries

In this section, the VDC approach [12], with its mathematical foundation, is introduced to be used for dynamics

modeling, controller design, and a stability analysis of the manipulator.

1) *Kinematics and Dynamics of a Rigid Body*: Let $\{\mathbf{A}\}$ be a three-dimensional orthogonal coordinate system, attached to a rigid body. Considering ${}^{\mathbf{A}}\mathbf{v} \in \mathbb{R}^3$ and ${}^{\mathbf{A}}\boldsymbol{\omega} \in \mathbb{R}^3$ as the linear and angular velocity vectors, expressed in frame $\{\mathbf{A}\}$, the linear/angular velocity vector of frame $\{\mathbf{A}\}$ is defined as:

$${}^{\mathbf{A}}\mathbf{V} \stackrel{\text{def}}{=} \begin{bmatrix} {}^{\mathbf{A}}\mathbf{v} \\ {}^{\mathbf{A}}\boldsymbol{\omega} \end{bmatrix} \in \mathbb{R}^6. \quad (1)$$

Similarly, let ${}^{\mathbf{A}}\mathbf{f} \in \mathbb{R}^3$ and ${}^{\mathbf{A}}\boldsymbol{\tau} \in \mathbb{R}^3$ be the force and moment vectors that are applied, respectively, and expressed in frame $\{\mathbf{A}\}$. Therefore, the force/moment vector in frame $\{\mathbf{A}\}$ is defined as:

$${}^{\mathbf{A}}\mathbf{F} \stackrel{\text{def}}{=} \begin{bmatrix} {}^{\mathbf{A}}\mathbf{f} \\ {}^{\mathbf{A}}\boldsymbol{\tau} \end{bmatrix} \in \mathbb{R}^6. \quad (2)$$

It should be clarified that in VDC, as a systematic approach, we must transform linear/angular velocity vector ($\mathbf{V} \in \mathbb{R}^6$) from the base of the robot to the end-effector and transform the force/moment vector ($\mathbf{F} \in \mathbb{R}^6$) from the end-effector to the base. Now, consider frame $\{\mathbf{B}\}$ to be attached to the same rigid body. Consequently, we can transform the linear/angular velocity vector and force/moment vector between these two frames, as follows:

$$\begin{cases} {}^{\mathbf{B}}\mathbf{V} = {}^{\mathbf{A}}\mathbf{U}_{\mathbf{B}}^T {}^{\mathbf{A}}\mathbf{V}, \\ {}^{\mathbf{A}}\mathbf{F} = {}^{\mathbf{A}}\mathbf{U}_{\mathbf{B}} {}^{\mathbf{B}}\mathbf{F}, \end{cases} \quad (3)$$

where ${}^{\mathbf{A}}\mathbf{U}_{\mathbf{B}} \in \mathbb{R}^{6 \times 6}$ denotes the transformation matrix from frame $\{\mathbf{B}\}$ to frame $\{\mathbf{A}\}$, as follows:

$${}^{\mathbf{A}}\mathbf{U}_{\mathbf{B}} = \begin{bmatrix} {}^{\mathbf{A}}\mathbf{R}_{\mathbf{B}} & \mathbf{0}_{3 \times 3} \\ ({}^{\mathbf{A}}\mathbf{r}_{\mathbf{AB}} \times) {}^{\mathbf{A}}\mathbf{R}_{\mathbf{B}} & {}^{\mathbf{A}}\mathbf{R}_{\mathbf{B}} \end{bmatrix}, \quad (4)$$

where ${}^{\mathbf{A}}\mathbf{R}_{\mathbf{B}} \in \mathbb{R}^{3 \times 3}$ is the rotation matrix from frame $\{\mathbf{B}\}$ to frame $\{\mathbf{A}\}$. Moreover, if ${}^{\mathbf{A}}\mathbf{r}_{\mathbf{AB}} = [r_x, r_y, r_z]^T$ is the vector from the origin of frame $\{\mathbf{A}\}$ to the origin of frame $\{\mathbf{B}\}$, expressed in frame $\{\mathbf{A}\}$, then ${}^{\mathbf{A}}\mathbf{r}_{\mathbf{AB}} \times \in \mathbb{R}^{3 \times 3}$ is a skew-symmetric matrix operator defined as:

$$({}^{\mathbf{A}}\mathbf{r}_{\mathbf{AB}} \times) = \begin{bmatrix} 0 & -r_z & r_y \\ r_z & 0 & -r_x \\ -r_y & r_x & 0 \end{bmatrix}. \quad (5)$$

The net force/moment vectors of the rigid body in frame $\{\mathbf{A}\}$, defined as ${}^{\mathbf{A}}\mathbf{F}^* \in \mathbb{R}^6$, are calculated based on the rigid body's dynamics as:

$$\mathbf{M}_{\mathbf{A}} \frac{d}{dt} ({}^{\mathbf{A}}\mathbf{V}) + \mathbf{C}_{\mathbf{A}} {}^{\mathbf{A}}\mathbf{V} + \mathbf{G}_{\mathbf{A}} = {}^{\mathbf{A}}\mathbf{F}^*, \quad (6)$$

where $\mathbf{M}_{\mathbf{A}} \in \mathbb{R}^{6 \times 6}$ is the mass matrix, $\mathbf{C}_{\mathbf{A}} \in \mathbb{R}^{6 \times 6}$ denotes the matrix of coriolis and centrifugal terms, and $\mathbf{G}_{\mathbf{A}} \in \mathbb{R}^6$ corresponds to the gravity terms.

Property 1: Consider the rigid body dynamics described in (6). The following property can be established:

$$\tilde{\mathbf{Y}}_{\mathbf{A}} \theta_{\mathbf{A}} = \mathbf{M}_{\mathbf{A}} \frac{d}{dt} ({}^{\mathbf{A}}\mathbf{V}) + \mathbf{C}_{\mathbf{A}} {}^{\mathbf{A}}\mathbf{V} + \mathbf{G}_{\mathbf{A}}, \quad (7)$$

where $\tilde{\mathbf{Y}}_{\mathbf{A}}({}^{\mathbf{A}}\dot{\mathbf{V}}, {}^{\mathbf{A}}\mathbf{V}) \in \mathbb{R}^{6 \times 10}$ denotes the regressor matrix and $\theta_{\mathbf{A}}(m, {}^{\mathbf{A}}\mathbf{r}_{\mathbf{AB}}, I_{\mathbf{A}})$ is the corresponding inertial parameter vector, as defined in [54].

2) *Required Linear/Angular Velocity and Force/Moment Vectors*: In VDC, the required velocity differs from the desired velocity. While the desired velocity represents the intended motion, the required velocity incorporates this target along with additional terms that consider such control errors as position error. Therefore, the required joint velocities are defined as follows:

$$\begin{cases} \dot{q}_r = \dot{q}_d + \lambda(q_d - q) & \text{(For revolute joints)} \\ \dot{x}_r = \dot{x}_d + \lambda(x_d - x) & \text{(For prismatic joints)} \end{cases} \quad (8)$$

where λ is the positive control parameter; \dot{q}_d and \dot{x}_d are the desired angular and linear velocities, respectively; q_d and x_d are the desired angular and linear positions, and q and x are the measured angular and linear positions.

Once the required joint velocities are determined, the corresponding required linear/angular velocity vector in any frame $\{\mathbf{A}\}$, denoted as ${}^{\mathbf{A}}\mathbf{V}_r \in \mathbb{R}^6$, can be computed, which will be described in details subsequently. Eventually, once the required linear/angular velocity vectors are determined, the required net force/moment vector in frame $\{\mathbf{A}\}$, defined as ${}^{\mathbf{A}}\mathbf{F}_r^* \in \mathbb{R}^6$, is delineated by:

$${}^{\mathbf{A}}\mathbf{F}_r^* = Y_A \hat{\theta}_A + \mathbf{K}_A ({}^{\mathbf{A}}\mathbf{V}_r - {}^{\mathbf{A}}\mathbf{V}), \quad (9)$$

where $\mathbf{K}_A \in \mathbb{R}^{6 \times 6}$ is a positive-definite gain matrix, $Y_A ({}^{\mathbf{A}}\dot{\mathbf{V}}_r, {}^{\mathbf{A}}\mathbf{V}_r) \in \mathbb{R}^{6 \times 10}$ denotes the regressor matrix in the sense of Property (1), and $\hat{\theta}_A$ is the estimation of θ_A , explained in the following.

3) *Natural Adaptation Law*: For a rigid body represented by frame $\{\mathbf{A}\}$, there exists a unique set of inertial parameters $\theta_A \in \mathbb{R}^{10}$ that satisfy the conditions of physical consistency. As elaborated in [54], there exists a linear map $f: \mathbb{R}^{10} \rightarrow S(4)$ such that:

$$f(\theta_A) = \mathcal{L}_A = \begin{bmatrix} 0.5 \text{tr}(I_A) \cdot \mathbf{1} - I_A & h_A \\ h_A^\top & m_A \end{bmatrix}, \quad (10)$$

$$f^{-1}(\mathcal{L}_A) = \theta_A(m_A, h_A, \text{tr}(\Sigma_A) \cdot \mathbf{1} - \Sigma_A), \quad (11)$$

where m_A , h_A , and I_A denote the mass, first moment of mass, and the rotational inertia tensor, respectively. The matrix $\mathcal{L}_A \in S(4)$ is referred to as the pseudo-inertia matrix, with $S(4)$ denoting the space of real symmetric 4×4 matrices, and $\Sigma_A = 0.5 \text{tr}(I_A) - I_A$.

Given a true pseudo-inertia matrix \mathcal{L}_A and its estimate $\hat{\mathcal{L}}_A$, a Lyapunov function can be formulated using the Bregman divergence based on the log-determinant function, as follows:

$$\mathcal{D}_F(\mathcal{L}_A \parallel \hat{\mathcal{L}}_A) = \log \frac{|\hat{\mathcal{L}}_A|}{|\mathcal{L}_A|} + \text{tr}(\hat{\mathcal{L}}_A^{-1} \mathcal{L}_A) - 4, \quad (12)$$

with the time derivative of (12) given by:

$$\dot{\mathcal{D}}_F(\mathcal{L}_A \parallel \hat{\mathcal{L}}_A) = \text{tr} \left(\hat{\mathcal{L}}_A^{-1} \dot{\hat{\mathcal{L}}}_A \hat{\mathcal{L}}_A^{-1} \tilde{\mathcal{L}}_A \right), \quad (13)$$

where $\tilde{\mathcal{L}}_A = \hat{\mathcal{L}}_A - \mathcal{L}_A$ represents the estimation error. Consequently, the natural adaptation law (NAL) is obtained by:

$$\dot{\hat{\mathcal{L}}}_A = \frac{1}{\gamma} \hat{\mathcal{L}}_A \mathcal{S}_A \hat{\mathcal{L}}_A, \quad (14)$$

where $\gamma > 0$ is the adaptation gain applied uniformly across all rigid bodies, and $\gamma_0 > 0$ is a small positive scalar. The matrix \mathcal{S}_A is a uniquely defined symmetric matrix as described in [14, Appendix D].

4) *Virtual Power Flow (VPF) and Virtual Stability*:

Definition 1: Relative to frame $\{\mathbf{A}\}$, the VPF is defined as the inner product between the linear/angular velocity error and the force/moment error vectors, as introduced in [12]:

$$p_A = ({}^{\mathbf{A}}\mathbf{V}_r - {}^{\mathbf{A}}\mathbf{V})^T ({}^{\mathbf{A}}\mathbf{F}_r - {}^{\mathbf{A}}\mathbf{F}), \quad (15)$$

where ${}^{\mathbf{A}}\mathbf{V}_r \in \mathbb{R}^6$ and ${}^{\mathbf{A}}\mathbf{F}_r \in \mathbb{R}^6$ denote the required linear/angular velocity and force/moment vectors, respectively, corresponding to the actual vectors ${}^{\mathbf{A}}\mathbf{V}$ and ${}^{\mathbf{A}}\mathbf{F}$.

Definition 2: A non-negative accompanying function $\nu(t) \in \mathbb{R}$ is a piecewise continuously differentiable function defined for all $t \in \mathbb{R}^+$, satisfying $\nu(0) < \infty$, and possessing a well-defined time derivative $\dot{\nu}(t)$ almost everywhere.

Definition 3: A subsystem obtained through decomposition is said to be virtually stable if there exists a non-negative accompanying function $\nu(t)$, such that its time derivative satisfies the inequality [12]:

$$\dot{\nu}(t) \leq -B(t) + \sum_{\{\mathbf{A}\} \in \Phi} p_A - \sum_{\{\mathbf{C}\} \in \Psi} p_C, \quad (16)$$

where $B(t)$ is a positive function, Φ and Ψ represent the sets of driven and driving virtual cutting frames of this subsystem, respectively, and p_A and p_C are the corresponding VPFs in these frames.

Theorem 1: Consider a complex robotic structure decomposed into subsystems with rigid body subsystem representation (6). If each of the constituent subsystems satisfies the virtual stability condition specified in Definition 3, then the overall system is stable [12].

B. Integrated Dynamic Model of the EMLA

The EMLA investigated in this study consists of a PMSM driving a linear output via a gearbox and a lead screw [55]. This section describes the EMLA dynamics from the electrical domain of the motor to the mechanical domain of force generation. The electrical behavior of the PMSM in the synchronous dq reference frame is governed by the following voltage and flux linkage relations [56]:

$$\begin{cases} v_d = R_s i_d + \frac{d\lambda_d}{dt} - p \dot{\theta}_m \lambda_q \\ v_q = R_s i_q + \frac{d\lambda_q}{dt} + p \dot{\theta}_m \lambda_d \end{cases} \quad (17)$$

where v_d , v_q and i_d , i_q represent the stator voltages and currents in the dq frame, R_s is the stator resistance, $\dot{\theta}_m$ is the mechanical angular speed, and λ_d , λ_q are the corresponding flux linkages. For surface-mounted configurations, where $L_d = L_q$, the flux linkages simplify to $\lambda_d = L_d i_d + \lambda_m$ and $\lambda_q = L_q i_q$, with λ_m being the flux linkage due to the permanent magnets. To transition into the mechanical domain, the electromagnetic torque generated by the PMSM is expressed as [57]:

$$\tau_e = \frac{3}{2} p (\lambda_d i_q - \lambda_q i_d) \quad (18)$$

where p denotes the number of pole pairs. Meanwhile, the mechanical dynamics of the PMSM rotor are governed by [58]:

$$J_m \ddot{\theta}_m = \tau_e - \tau'_s - C_m \dot{\theta}_m - \tau_C \quad (19)$$

where J_m is the motor inertia, C_m is the viscous damping coefficient, τ_C is the Coulomb friction, and τ'_s denotes the torque reflected to the motor shaft from the downstream screw-side load. The motor output is connected to a shaft via a gearbox with reduction ratio N_{gear} and efficiency η_{gear} , and the screw shaft angular velocity $\dot{\theta}_s$ is related to the motor shaft speed $\dot{\theta}_m$ as follows:

$$\dot{\theta}_s = \frac{1}{N_{\text{gear}}} \dot{\theta}_m \quad (20)$$

and the torque at the screw shaft is determined by:

$$\tau_s = \eta_{\text{gear}} N_{\text{gear}} \left(\tau_e - C_m \dot{\theta}_m \right) \quad (21)$$

Rotary-to-linear motion is achieved through a lead screw, characterized by its lead ρ in meters per revolution. The linear velocity of the moving nut \dot{x}_n is related to the screw shaft angular velocity, as follows:

$$\dot{x}_n = \frac{\rho}{2\pi} \dot{\theta}_s \quad (22)$$

To model the elastic and damping effects between the screw nut and the actuator rod, a two-mass system is introduced. This formulation captures the relative compliance between the nut and rod, which may arise due to mechanical backlash, preload effects, or structural flexibilities in the screw-nut interface. The back-drive torque τ_{bd} resulting from relative motion between the nut and the rod is given by:

$$\tau_{\text{bd}} = \frac{\rho}{2\pi} [C_b(\dot{x}_n - \dot{x}) + K_b(x_n - x)] \quad (23)$$

where x_n and \dot{x}_n are the nut's position and velocity, x and \dot{x} are the rod's position and velocity, and C_b and K_b denote the equivalent damping and stiffness terms of the screw-nut system, respectively. Thus, the rotational dynamics of the screw shaft become:

$$J_s \ddot{\theta}_s + C_s \dot{\theta}_s = \tau_s - \tau_{\text{bd}} \quad (24)$$

The actuator rod, driven via the screw nut, follows the second-order linear equation, as follows:

$$M_{\text{act}} \ddot{x} + C_{\text{act}} \dot{x} + C_b(\dot{x} - \dot{x}_n) + K_b(x - x_n) = -F_{\text{ext}} \quad (25)$$

where M_{act} and C_{act} denote the effective mass and damping of the actuator rod and its driven components, respectively, and F_{ext} represents the external force acting on the actuator output. The equivalent stiffness K_b of the screw-nut-rod transmission is modeled as the parallel combination of elastic elements, including shaft flexibility, bearing and interface compliance, and torsional deformation [59]:

$$K_b = \left(\frac{\ell_s}{K_s} + \frac{1}{2K_{\text{br}}} + \frac{1}{K_n} + \frac{1}{K_r} + \frac{\rho^2 x}{4\pi^2 K_{\text{rot}}} \right)^{-1} \quad (26)$$

where the terms K_s , K_{br} , K_n , K_r , and K_{rot} represent the stiffnesses of the screw shaft, bearing, nut interface, rod, and the torsional stiffness of the rotating parts, respectively. The term ℓ_s denotes the effective length of the screw shaft under axial deformation and is defined as:

$$\ell_s = \frac{x(L_s - x)}{L_s} \quad (27)$$

where x is the actuator rod displacement and L_s is the axial distance between the screw shaft bearings. The overall efficiency of the EMLA is defined later in Section III-B as the ratio of the mechanical output power to electrical input power.

III. SYSTEM MODELING

A. Analytical HDRM Model

This section presents the kinematic and dynamic modeling of the manipulator, a 6-DOF electric HDRM. As illustrated in Fig. 1, the manipulator is segmented into four main components: the base, lift, tilt, and wrist. Given that the system incorporates both three-bar and four-bar mechanisms, use of the VDC offers a generalized and systematic framework for deriving equations of motion, applicable to a wide range of manipulator architectures.

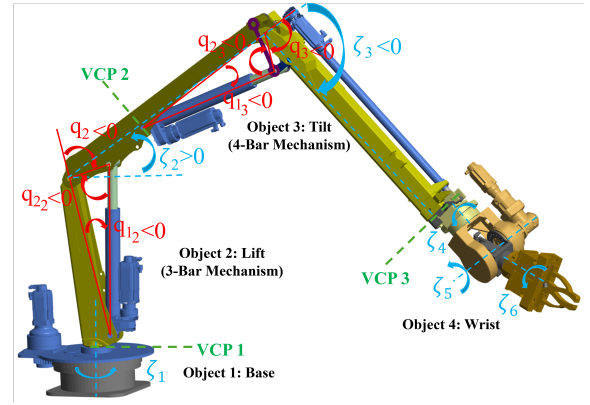


Fig. 1. Schematic of the electric HDRM.

1) *HDRM Kinematic Formulation:* The manipulator's kinematics are derived individually for each of its four structural segments. The VDC frames in conjunction with the virtual cutting points (VCPs), are presented in Fig. (2), though it should be mentioned that according to the VDC approach, linear/angular velocity vectors are derived from the base of the robot to the wrist. In the remainder of this paper, the following equation is used based on the VDC:

$$\begin{cases} x_f = [1, 0, 0, 0, 0, 0]^T, \\ y_f = [0, 1, 0, 0, 0, 0]^T, \\ z_f = [0, 0, 1, 0, 0, 0]^T, \\ x_\tau = [0, 0, 0, 1, 0, 0]^T, \\ y_\tau = [0, 0, 0, 0, 1, 0]^T, \\ z_\tau = [0, 0, 0, 0, 0, 1]^T. \end{cases} \quad (28)$$

• Base Motion:

According to the VDC approach, the linear/angular velocity vector for the first object is calculated as follows:

$$\mathbf{T}_1 \mathbf{V} = \mathbf{y}_\tau \dot{\zeta}_1 + \mathbf{B}_1 \mathbf{U}_{\mathbf{T}_1}^T \mathbf{B}_1 \mathbf{V}, \quad (29)$$

where $\mathbf{B}_1 \mathbf{V}$ denotes the ground and is a zero vector in our study. In the next step, the linear/angular velocity vector of the second object is calculated, using the following equation:

$$\mathbf{B}_{c2} \mathbf{V} = \mathbf{T}_1 \mathbf{U}_{\mathbf{B}_{c2}}^T \mathbf{T}_1 \mathbf{V}. \quad (30)$$

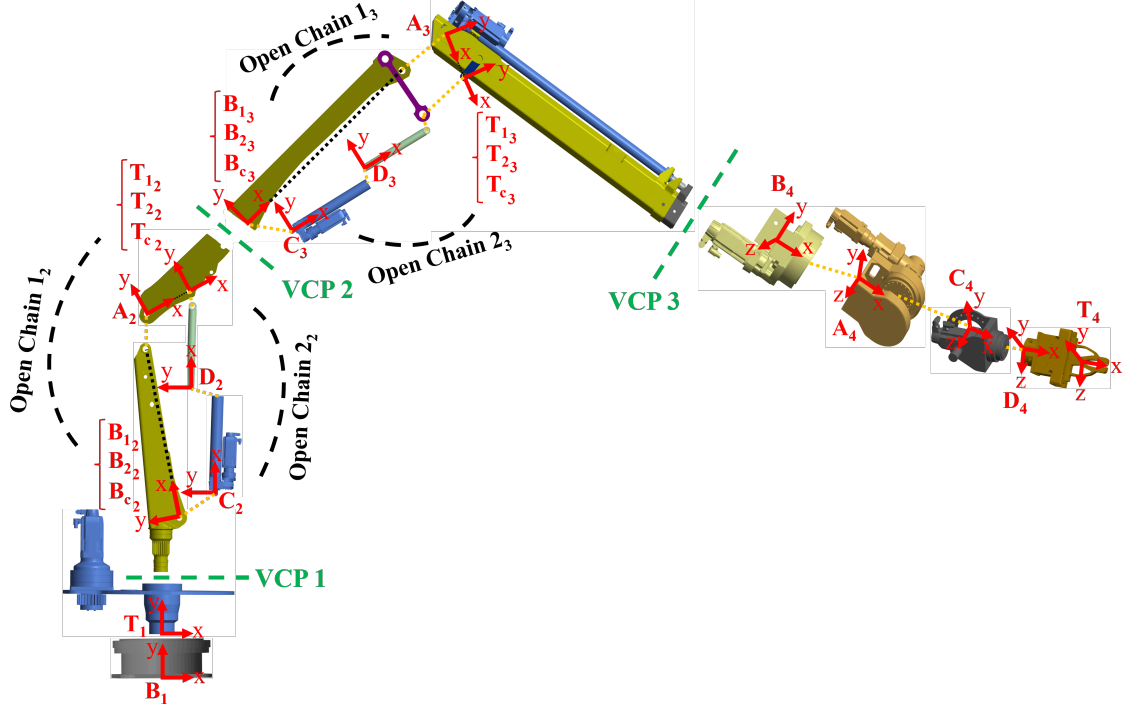


Fig. 2. VDC frames of the manipulator.

- Lift Motion (Three-Bar Mechanism):

In this section, the kinematics of the lift motion, which is a three-bar mechanism, are derived. As it is the second object, all variables have a subscript of 2. The schematic view of the second object is shown in Fig. (3), though it should be noted that the signs of the angles q_2 , q_{12} , q_{22} , and ζ_2 are defined counterclockwise. Therefore, we have:

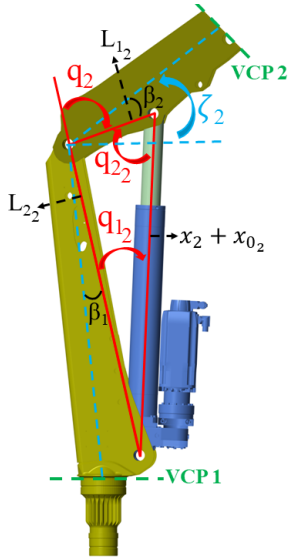


Fig. 3. Schematic of the lift (3-bar mechanism).

$$\beta_1 + (\pi + q_2) + (\beta_2 - \zeta_2) = \frac{\pi}{2}, \quad (31)$$

where β_1 and β_2 are two positive constant angles. Therefore, the lift angle (q_2) can be derived based on the measurement from the sensor (ζ_2), as follows:

$$q_2 = \left(-\frac{\pi}{2} - \beta_1 - \beta_2\right) + \zeta_2. \quad (32)$$

Based on the law of cosines, we have:

$$\begin{cases} x_2 = \sqrt{L_{12}^2 + L_{22}^2 + 2L_{12}L_{22}\cos q_2} - x_{02}, \\ q_{12} = -\arccos\left(\frac{L_{12}^2 - (x_2 + x_{02})^2 - L_{22}^2}{-2(x_2 + x_{02})L_{22}}\right), \\ q_{22} = -\arccos\left(\frac{L_{22}^2 - (x_2 + x_{02})^2 - L_{12}^2}{-2(x_2 + x_{02})L_{12}}\right). \end{cases} \quad (33)$$

By differentiating (33), the velocity equations are derived as follows:

$$\begin{cases} \dot{x}_2 = -\frac{L_{12}L_{22}\sin q_2}{x_2 + x_{02}}\dot{q}_2, \\ \dot{q}_{12} = -\frac{(x_2 + x_{02}) - L_{22}\cos q_{12}}{(x_2 + x_{02})L_{22}\sin q_{12}}\dot{x}_2, \\ \dot{q}_{22} = -\frac{(x_2 + x_{02}) - L_{12}\cos q_{22}}{(x_2 + x_{02})L_{12}\sin q_{22}}\dot{x}_2, \end{cases} \quad (34)$$

where $\dot{q}_2 = \dot{\zeta}_2$, based on (32). It should be noted that (33) and (34) define the relation between the lift passive joint and the EMLA motion.

According to the VDC approach, the linear/angular velocity vectors for the open chain 1₂ are calculated as follows:

$$\begin{cases} \mathbf{A}_2 \mathbf{V} = \mathbf{z}_r \dot{q}_2 + \mathbf{B}_{12} \mathbf{U}_{\mathbf{A}_2}^T \mathbf{B}_{12} \mathbf{V}, \\ \mathbf{T}_{12} \mathbf{V} = \mathbf{A}_2 \mathbf{U}_{\mathbf{T}_{12}}^T \mathbf{A}_2 \mathbf{V}, \end{cases} \quad (35)$$

Similarly, for the open chain 2₂, we have:

$$\begin{cases} \mathbf{C}_2 \mathbf{V} = \mathbf{z}_\tau \dot{q}_{12} + \mathbf{B}_{22} \mathbf{U}_{\mathbf{C}_2}^T \mathbf{B}_{22} \mathbf{V}, \\ \mathbf{D}_2 \mathbf{V} = \mathbf{x}_f \dot{x}_2 + \mathbf{C}_2 \mathbf{U}_{\mathbf{D}_2}^T \mathbf{C}_2 \mathbf{V}, \\ \mathbf{T}_{22} \mathbf{V} = \mathbf{z}_\tau \dot{q}_{22} + \mathbf{D}_2 \mathbf{U}_{\mathbf{T}_{22}}^T \mathbf{D}_2 \mathbf{V}, \end{cases} \quad (36)$$

Because the beginning and end points of the open chains 1₂ and 2₂ coincide, the following constraints apply:

$$\begin{cases} \mathbf{B}_{12} \mathbf{V} = \mathbf{B}_{22} \mathbf{V} = \mathbf{B}_{c2} \mathbf{V}, \\ \mathbf{T}_{12} \mathbf{V} = \mathbf{T}_{22} \mathbf{V} = \mathbf{T}_{c2} \mathbf{V}, \end{cases} \quad (37)$$

Eventually, the linear/angular velocity vector for the base of the third object is calculated as follows:

$$\mathbf{B}_{c3} \mathbf{V} = \mathbf{T}_{c2} \mathbf{U}_{\mathbf{B}_{c3}}^T \mathbf{T}_{c2} \mathbf{V}. \quad (38)$$

- Tilt Motion (Four-Bar Mechanism):

In this section, we derive the kinematic equations governing tilt motion, which is a four-bar linkage mechanism. As this corresponds to the third object in the system, all related variables carry the subscript 3. Note that the angles q_3 , q_{13} , q_{23} , and ζ_3 are defined as positive in the counterclockwise direction.

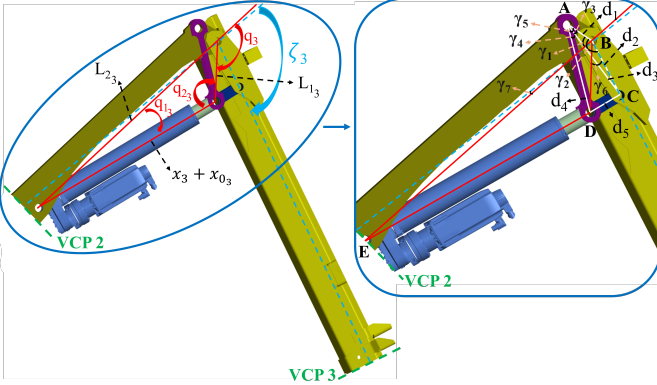


Fig. 4. Schematic of the tilt (4-bar mechanism).

Referring to Fig. (4), the geometric relationships within triangle ABC yield:

$$\begin{cases} \gamma_2 = \gamma_1 + (\pi + \zeta_3), \\ d_3 = \sqrt{d_1^2 + d_2^2 - 2d_1d_2 \cos \gamma_2}, \\ \gamma_3 = \arcsin \left(\frac{d_2}{d_3} \sin \gamma_2 \right), \end{cases} \quad (39)$$

where γ_1 is a constant angle, ζ_3 denotes the angle measured by the sensor, and d_1 and d_2 represent constant lengths. From triangle ACD , it follows that:

$$\gamma_4 = \arccos \left(\frac{d_3^2 + d_4^2 - d_5^2}{2d_3d_4} \right). \quad (40)$$

The parameters d_4 and d_5 are constant lengths known from the mechanism's geometry. Now, by considering triangle ABD , we obtain:

$$\begin{cases} \gamma_5 = \gamma_3 + \gamma_4, \\ L_{13} = \sqrt{d_1^2 + d_4^2 - 2d_1d_4 \cos \gamma_5}. \end{cases} \quad (41)$$

Here, L_{13} denotes a key length that plays a critical role in the following analysis. Now, by considering triangle CDE , we obtain:

$$\gamma_6 = \arccos \left(\frac{d_2^2 + L_{13}^2 - d_5^2}{2d_2L_{13}} \right). \quad (42)$$

Given γ_6 from Equation (42) and the sensor-measured angle ζ_3 , it follows that:

$$q_3 = -\gamma_7 - \gamma_6 + \zeta_3, \quad (43)$$

where γ_7 is a constant angle.

Similar to the lift motion, using the law of cosines, we have:

$$\begin{cases} x_3 = \sqrt{L_{13}^2 + L_{23}^2 + 2L_{13}L_{23} \cos q_3} - x_{03}, \\ q_{13} = -\arccos \left(\frac{L_{13}^2 - (x_3 + x_{03})^2 - L_{23}^2}{-2(x_3 + x_{03})L_{23}} \right), \\ q_{23} = -\arccos \left(\frac{L_{23}^2 - (x_3 + x_{03})^2 - L_{13}^2}{-2(x_3 + x_{03})L_{13}} \right). \end{cases} \quad (44)$$

Now, by differentiating (44), using the geometric parameters from (39) to (43), the variables \dot{x}_3 , \dot{q}_3 , \dot{q}_{13} , and \dot{q}_{23} are calculated.

Based on VDC, the linear/angular velocity vectors corresponding to the open chain 1₃ are obtained as follows:

$$\begin{cases} \mathbf{A}_3 \mathbf{V} = \mathbf{z}_\tau \dot{q}_3 + \mathbf{B}_{13} \mathbf{U}_{\mathbf{A}_3}^T \mathbf{B}_{13} \mathbf{V}, \\ \mathbf{T}_{13} \mathbf{V} = \mathbf{A}_3 \mathbf{U}_{\mathbf{T}_{13}}^T \mathbf{A}_3 \mathbf{V}, \end{cases} \quad (45)$$

In a similar manner, the linear/angular velocity vectors for the open chain 2₃ are given by:

$$\begin{cases} \mathbf{C}_3 \mathbf{V} = \mathbf{z}_\tau \dot{q}_{13} + \mathbf{B}_{23} \mathbf{U}_{\mathbf{C}_3}^T \mathbf{B}_{23} \mathbf{V}, \\ \mathbf{D}_3 \mathbf{V} = \mathbf{x}_f \dot{x}_3 + \mathbf{C}_3 \mathbf{U}_{\mathbf{D}_3}^T \mathbf{C}_3 \mathbf{V}, \\ \mathbf{T}_{23} \mathbf{V} = \mathbf{z}_\tau \dot{q}_{23} + \mathbf{D}_3 \mathbf{U}_{\mathbf{T}_{23}}^T \mathbf{D}_3 \mathbf{V}, \end{cases} \quad (46)$$

As the initial and terminal points of the open chains 1₃ and 2₃ coincide, the following constraint equations must be satisfied:

$$\begin{cases} \mathbf{B}_{13} \mathbf{V} = \mathbf{B}_{23} \mathbf{V} = \mathbf{B}_{c3} \mathbf{V}, \\ \mathbf{T}_{13} \mathbf{V} = \mathbf{T}_{23} \mathbf{V} = \mathbf{T}_{c3} \mathbf{V}, \end{cases} \quad (47)$$

Finally, the linear/angular velocity vector at the base of the fourth object is computed as follows:

$$\mathbf{B}_4 \mathbf{V} = \mathbf{T}_{c3} \mathbf{U}_{\mathbf{B}_4}^T \mathbf{T}_{c3} \mathbf{V}. \quad (48)$$

- Wrist Motion:

At this stage, we proceed to derive the kinematic equations associated with the wrist mechanism. As the wrist constitutes the fourth element in the kinematic chain, all corresponding variables are denoted with the subscript 4 to maintain consistency in notation. The kinematic relationship from the wrist base frame, denoted as \mathbf{B}_4 , to the wrist tip frame, denoted as \mathbf{T}_4 , which corresponds to the end effector, is formulated as follows:

$$\begin{cases} \mathbf{A}_4 \mathbf{V} = \mathbf{x}_\tau \dot{\zeta}_4 + \mathbf{B}_4 \mathbf{U}_{\mathbf{A}_4}^T \mathbf{B}_4 \mathbf{V}, \\ \mathbf{C}_4 \mathbf{V} = \mathbf{z}_\tau \dot{\zeta}_5 + \mathbf{A}_4 \mathbf{U}_{\mathbf{C}_4}^T \mathbf{A}_4 \mathbf{V}, \\ \mathbf{D}_4 \mathbf{V} = \mathbf{x}_\tau \dot{\zeta}_6 + \mathbf{C}_4 \mathbf{U}_{\mathbf{D}_4}^T \mathbf{C}_4 \mathbf{V}, \\ \mathbf{T}_4 \mathbf{V} = \mathbf{D}_4 \mathbf{U}_{\mathbf{T}_4}^T \mathbf{D}_4 \mathbf{V}, \end{cases} \quad (49)$$

2) *HDRM Dynamic Formulation*: The dynamics of the manipulator are now formulated from the end-effector toward the base, following the principles of the VDC approach. With the linear/angular velocity vectors of each component obtained, we substitute them into (6) to compute the net force/moment vectors (\mathbf{F}^*) for each individual component. According to the VDC framework, the force/moment vectors are computed in a recursive manner, propagating from the wrist toward the base of the manipulator, as follows:

- Wrist Motion:

The dynamic behavior of the fourth component in the system, corresponding to the wrist, is described by the following equations:

$$\begin{cases} \mathbf{D}_4 \mathbf{F} = \mathbf{D}_4 \mathbf{F}^* + \mathbf{D}_4 \mathbf{U}_{T_4} \mathbf{T}_4 \mathbf{F}, \\ \mathbf{C}_4 \mathbf{F} = \mathbf{C}_4 \mathbf{F}^* + \mathbf{C}_4 \mathbf{U}_{D_4} \mathbf{D}_4 \mathbf{F}, \\ \mathbf{A}_4 \mathbf{F} = \mathbf{A}_4 \mathbf{F}^* + \mathbf{A}_4 \mathbf{U}_{C_4} \mathbf{C}_4 \mathbf{F}, \\ \mathbf{B}_4 \mathbf{F} = \mathbf{B}_4 \mathbf{F}^* + \mathbf{B}_4 \mathbf{U}_{A_4} \mathbf{A}_4 \mathbf{F}, \end{cases} \quad (50)$$

where $\mathbf{T}_4 \mathbf{F}$ denotes the force/moment vector exerted on the end-effector by the environment, which can include contributions from the payload.

- Tilt Motion (Four-Bar Mechanism):

Having obtained the force/moment vector at the base of the wrist (\mathbf{B}_4), we can now transfer it to the base of the tilt mechanism (\mathbf{B}_{c3}) using the following equation. A comprehensive derivation of this relation is provided in [17]:

$$\begin{aligned} \mathbf{B}_{c3} \mathbf{F} = & \mathbf{B}_{13} \mathbf{F}^* + \mathbf{B}_{13} \mathbf{U}_{A_3} \mathbf{A}_3 \mathbf{F}^* + \mathbf{B}_{23} \mathbf{U}_{C_3} \mathbf{C}_3 \mathbf{F}^* \\ & + \mathbf{B}_{23} \mathbf{U}_{C_3} \mathbf{C}_3 \mathbf{U}_{D_3} \mathbf{D}_3 \mathbf{F}^* + \mathbf{B}_{13} \mathbf{U}_{A_3} \mathbf{A}_3 \mathbf{U}_{B_4} \mathbf{B}_4 \mathbf{F}. \end{aligned} \quad (51)$$

Furthermore, the force exerted by the linear actuator (EMLA) in the tilt mechanism is computed as follows:

$$\begin{aligned} f_3 = & \mathbf{x}_f^T \mathbf{D}_3 \mathbf{F}^* - \frac{\mathbf{z}_\tau^T (\mathbf{A}_3 \mathbf{F}^* + \mathbf{A}_3 \mathbf{U}_{B_4} \mathbf{B}_4 \mathbf{F})}{L_{13} \sin q_{23}} \\ & - \frac{\mathbf{z}_\tau^T (\mathbf{C}_3 \mathbf{F}^* + \mathbf{D}_3 \mathbf{F}^*) + \mathbf{y}_f^T (\mathbf{D}_3 \mathbf{F}^*) (x_3 + x_{03} - l_{c3})}{(x_3 + x_{03}) \tan q_{23}}. \end{aligned} \quad (52)$$

- Lift Motion (Three-Bar Mechanism):

Similarly, the force/moment vector calculated at the base of the tilt joint (\mathbf{B}_{c3}) is subsequently mapped to the base of the lift mechanism (\mathbf{B}_{c2}) using the transformation equation presented below [17].

$$\begin{aligned} \mathbf{B}_{c2} \mathbf{F} = & \mathbf{B}_{12} \mathbf{F}^* + \mathbf{B}_{12} \mathbf{U}_{A_2} \mathbf{A}_2 \mathbf{F}^* + \mathbf{B}_{22} \mathbf{U}_{C_2} \mathbf{C}_2 \mathbf{F}^* \\ & + \mathbf{B}_{22} \mathbf{U}_{C_2} \mathbf{C}_2 \mathbf{U}_{D_2} \mathbf{D}_2 \mathbf{F}^* + \mathbf{B}_{12} \mathbf{U}_{A_2} \mathbf{A}_2 \mathbf{U}_{B_{c3}} \mathbf{B}_{c3} \mathbf{F}. \end{aligned} \quad (53)$$

The force generated by the linear actuator (EMLA) within the lift mechanism is determined using the following expression:

$$\begin{aligned} f_2 = & \mathbf{x}_f^T \mathbf{D}_2 \mathbf{F}^* - \frac{\mathbf{z}_\tau^T (\mathbf{A}_2 \mathbf{F}^* + \mathbf{A}_2 \mathbf{U}_{B_{c3}} \mathbf{B}_{c3} \mathbf{F})}{L_{12} \sin q_{22}} \\ & - \frac{\mathbf{z}_\tau^T (\mathbf{C}_2 \mathbf{F}^* + \mathbf{D}_2 \mathbf{F}^*) + \mathbf{y}_f^T (\mathbf{D}_2 \mathbf{F}^*) (x_2 + x_{02} - l_{c2})}{(x_2 + x_{02}) \tan q_{22}}. \end{aligned} \quad (54)$$

- Base Motion:

Given the force/moment vector $\mathbf{B}_{c2} \mathbf{F}$ from object 2, the corresponding force/moment vector at the base can be obtained using the following relation:

$$\mathbf{T}_1 \mathbf{F} = \mathbf{T}_1 \mathbf{F}^* + \mathbf{T}_1 \mathbf{U}_{B_{c2}} \mathbf{B}_{c2} \mathbf{F}. \quad (55)$$

Finally, the force generated by the EMLA contributing to the base motion is given by:

$$f_1 = \frac{1}{r_B} \mathbf{y}_\tau^T (\mathbf{T}_1 \mathbf{F}), \quad (56)$$

where r_B denotes the radius of the base mechanism.

B. Surrogate-Enhanced Hybrid Model of the EMLA

To complement the physics-based model described in the previous section, this study leverages experimental data to characterize the dynamic behavior of the EMLA under realistic operating conditions. A long-duration test campaign was conducted, during which the EMLA was driven across a wide range of loads (0–70 kN) and speeds (0–70 mm/s), as illustrated in Fig. 5. The recorded dataset includes syn-

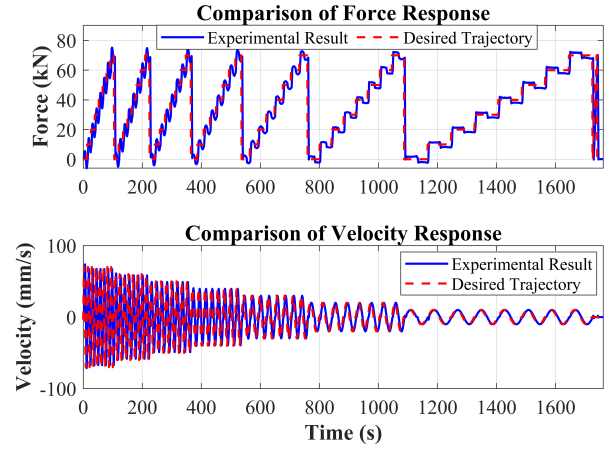


Fig. 5. Comparison of the experimental force and velocity responses with the desired trajectory.

chronized measurements of actuator output force (F_{ext}), linear velocity (\dot{x}), and motor-side electrical signals (v_d, v_q, i_d, i_q), from which the instantaneous mechanical output power and electrical input power were evaluated at each operating point. The EMLA efficiency $\eta_{\text{EMLA}}(\dot{\theta}_m, \tau_e)$ was then computed as follows:

$$\eta_{\text{EMLA}}(\dot{\theta}_m, \tau_e) = \frac{\dot{x}^\top F_{\text{ext}}}{\dot{\theta}_m^\top \tau_e + P_{\text{loss}}(v_d, v_q, i_d, i_q)} \quad (57)$$

where P_{loss} represents cumulative motor losses. As the raw efficiency values are non-differentiable and computationally expensive to evaluate in real-time applications, a data-driven surrogate model was developed. A lightweight deep neural network (DNN) was trained on the experimental dataset to approximate the actuator behavior. The DNN receives PMSM torque (τ_e) and angular velocity ($\dot{\theta}_m$) as inputs and predicts the corresponding actuator force (\hat{F}_{ext}) and linear velocity ($\hat{\dot{x}}$), and the inferred outputs enable reconstruction of the mechanical

power (\hat{P}_{out}) and estimation of the predicted efficiency as follows:

$$\begin{aligned} \begin{bmatrix} \hat{F}_{\text{ext}} \\ \hat{\dot{x}} \end{bmatrix} &= \mathcal{F}_{\text{DNN}} \left(\begin{bmatrix} \tau_e \\ \dot{\theta}_m \end{bmatrix} \right), \\ \hat{P}_{\text{out}} &= \hat{\dot{x}}^\top \cdot \hat{F}_{\text{ext}}, \\ P_{\text{in}} &= \dot{\theta}_m^\top \cdot \tau_e, \\ P_{\text{loss}} &= P_{\text{sw}} + P_{\text{cu}} + P_{\text{core}} + P_{\text{mech}}, \\ \hat{\eta}_{\text{EMLA}} &= \begin{cases} \frac{\hat{P}_{\text{out}}}{P_{\text{in}} + P_{\text{loss}}}, & \text{if } \tau_e > 0 \text{ and } \dot{\theta}_m > 0 \quad (\text{Q-I}) \\ \frac{P_{\text{in}} - P_{\text{loss}}}{\hat{P}_{\text{out}}}, & \text{if } \tau_e > 0 \text{ and } \dot{\theta}_m < 0 \quad (\text{Q-IV}) \\ \text{NaN}, & \text{otherwise} \end{cases} \end{aligned} \quad (58)$$

with P_{sw} , P_{cu} , P_{core} , and P_{mech} denoting the switching losses, copper-conduction losses, core losses including hysteresis and eddy currents, and mechanical losses including windage and bearing friction of the PMSM [60], [61]. The final network architecture consisted of a feedforward DNN with five hidden layers with sizes [64, 48, 32, 16, 8], trained using the Levenberg–Marquardt (`trainlm`) algorithm. A `mapminmax` normalization strategy was applied to both inputs and targets, and the model was trained for 1,000 epochs with early stopping patience set to 30 validation failures. The dataset was split into training, validation, and test sets using a 70:20:10 ratio. The DNN function $\mathcal{F}_{\text{DNN}}(x)$ can be structurally expressed as:

$$\hat{y} = \mathcal{F}_{\text{DNN}}(x) = \mathbf{W}_L \sigma_{L-1} \left(\cdots \sigma_2 \left(\mathbf{W}_2 \sigma_1 (\mathbf{W}_1 x + \mathbf{b}_1) + \mathbf{b}_2 \right) \cdots \right) + \mathbf{b}_L. \quad (59)$$

The objective function minimized was the mean squared error (MSE):

$$\mathcal{L}_{\text{MSE}} = \frac{1}{N} \sum_{i=1}^N (y_i - \hat{y}_i)^2, \quad (60)$$

where y_i and \hat{y}_i denote the true and predicted values of force and velocity. The trained DNN demonstrated an excellent predictive capability in reproducing both force and velocity responses, as illustrated in Fig. 6. Meanwhile, the trained model exhibited high accuracy, with correlation values exceeding $R > 0.995$ across the training, validation, and test subsets. The final model achieved training, validation, and test MSEs of 0.00013, 0.00476, and 0.00219, respectively, confirming low overfitting and strong generalization across the operating range.

Rather than replacing the physics-based model outright, the DNN is trained to estimate the residual dynamics not captured by the analytical formulation, such as unmodeled losses and nonlinearities [62], thereby refining the predicted force, velocity, and efficiency. The resulting hybrid model combines analytical predictions with data-driven corrections using formulation in (61), where each final output is computed as the sum of the physics-based estimate and a scaled neural residual. The coefficient $\alpha \in [0, 1]$ governs the influence of the

correction, and this structure ensures the hybrid model remains physically interpretable and dynamically consistent, while achieving high empirical accuracy suitable for integration into real-time control and an energy-aware simulation:

$$\begin{cases} F_{\text{hyb}} = F_{\text{ext}}(\dot{\theta}_m, \tau_e) + \alpha \left(\hat{F}_{\text{ext}} - F_{\text{ext}}(\dot{\theta}_m, \tau_e) \right), \\ \dot{x}_{\text{hyb}} = \dot{x}(\dot{\theta}_m, \tau_e) + \alpha \left(\hat{\dot{x}} - \dot{x}(\dot{\theta}_m, \tau_e) \right), \\ \eta_{\text{hyb}} = \eta_{\text{EMLA}}(\dot{\theta}_m, \tau_e) + \alpha \left(\hat{\eta}_{\text{EMLA}} - \eta_{\text{EMLA}}(\dot{\theta}_m, \tau_e) \right) \end{cases} \quad (61)$$

Finally, Fig. 7 illustrates the resulting surrogate-enhanced efficiency map that reflects the actuator's performance across the full range of operating conditions, derived from the hybrid formulation in (61). The resulting hybrid EMLA model is embedded into the VDC framework and is used to simulate the full 6-DoF all-electric robotic manipulator.

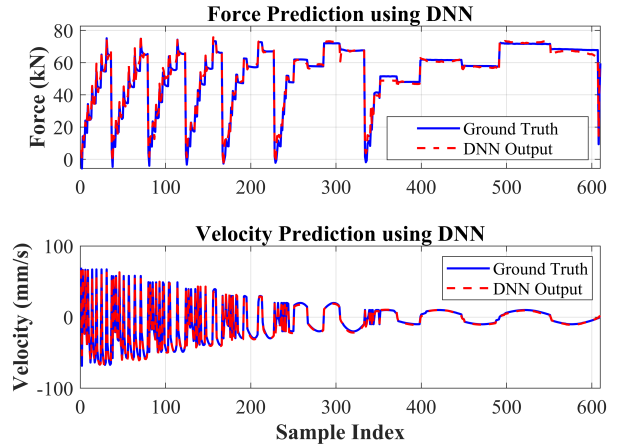


Fig. 6. Predicted versus ground-truth force and velocity responses of the EMLA using a trained deep neural network (DNN).

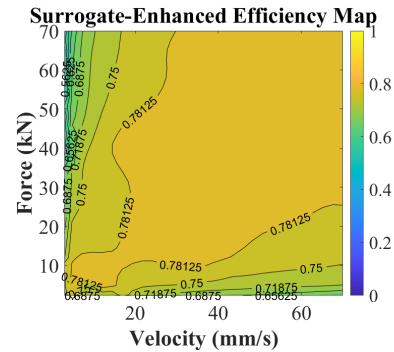


Fig. 7. Surrogate-enhanced efficiency map of the EMLA, combining physics-based modeling with DNN predictions. The map illustrates actuator efficiency across varying load forces and linear velocities, capturing both model-driven dynamics and experimentally-informed nonlinearities.

IV. CONTROL

Building upon the dynamic models presented earlier, this section derives the linear/angular velocity vectors, as well as

the corresponding force/moment vectors, required for control within the VDC framework.

First, consider the relationship between the task space and joint space, expressed using the Denavit–Hartenberg (DH) convention, as follows:

$$\dot{\mathbf{\Pi}} = \mathbf{J}\dot{\mathbf{\Theta}}, \quad (62)$$

where $\dot{\mathbf{\Pi}} \in \mathbb{R}^6$ denotes the linear/angular velocity vector of the end-effector in Cartesian space, $\mathbf{J} \in \mathbb{R}^{6 \times 6}$ is the Jacobian matrix, and $\mathbf{\Theta} = [\zeta_1, \zeta_2, \zeta_3, \zeta_4, \zeta_5, \zeta_6]^T$ represents the joint angle vector. Given a desired end-effector velocity $\dot{\mathbf{\Pi}}_d$ in Cartesian space, the required joint velocities can be computed using the closed-loop inverse kinematics (CLIK) method, as follows [63]:

$$\dot{\mathbf{\Theta}}_r = \mathbf{J}^{-1}(\dot{\mathbf{\Pi}}_d + \mathbf{\Lambda}(\mathbf{\Pi}_d - \mathbf{\Pi})), \quad (63)$$

where $\mathbf{\Lambda} \in \mathbb{R}^{6 \times 6}$ is a constant positive-definite matrix.

A. VDC Controller Design for the Manipulator (High-Level)

1) *Required Linear/Angular Velocity Vectors*: Now that the required joint velocities have been obtained from (63), the corresponding linear/angular velocity vectors can be derived by substituting the required velocity vectors into the equations presented in the modeling chapter (see Section III-A1).

- Base Motion:

$$\mathbf{T}_1 \mathbf{V}_r = \mathbf{y}_r \dot{\zeta}_{1_r} + \mathbf{B}_1 \mathbf{U}_{\mathbf{T}_1}^T \mathbf{B}_1 \mathbf{V}_r, \quad (64)$$

$$\mathbf{B}_{c2} \mathbf{V}_r = \mathbf{T}_1 \mathbf{U}_{\mathbf{B}_{c2}}^T \mathbf{T}_1 \mathbf{V}_r. \quad (65)$$

where $\dot{\zeta}_{1_r}$ is derived from (63).

- Lift Motion:

$$\begin{cases} \mathbf{A}_2 \mathbf{V}_r = \mathbf{z}_r \dot{q}_{2_r} + \mathbf{B}_{12} \mathbf{U}_{\mathbf{A}_2}^T \mathbf{B}_{12} \mathbf{V}_r, \\ \mathbf{T}_{12} \mathbf{V}_r = \mathbf{A}_2 \mathbf{U}_{\mathbf{T}_{12}}^T \mathbf{A}_2 \mathbf{V}_r, \end{cases} \quad (66)$$

$$\begin{cases} \mathbf{C}_2 \mathbf{V}_r = \mathbf{z}_r \dot{q}_{12_r} + \mathbf{B}_{22} \mathbf{U}_{\mathbf{C}_2}^T \mathbf{B}_{22} \mathbf{V}_r, \\ \mathbf{D}_2 \mathbf{V}_r = \mathbf{x}_f \dot{x}_{2_r} + \mathbf{C}_2 \mathbf{U}_{\mathbf{D}_2}^T \mathbf{C}_2 \mathbf{V}_r, \\ \mathbf{T}_{22} \mathbf{V}_r = \mathbf{z}_r \dot{q}_{22_r} + \mathbf{D}_2 \mathbf{U}_{\mathbf{T}_{22}}^T \mathbf{D}_2 \mathbf{V}_r, \end{cases} \quad (67)$$

where \dot{x}_{2_r} , \dot{q}_{2_r} , \dot{q}_{12_r} , and \dot{q}_{22_r} are readily obtained by substituting $\dot{\zeta}_{2_r}$ from (63) into (34). Then, the required linear/angular velocity vector at the base of the next object (tilt) is obtained as follows:

$$\mathbf{B}_{c3} \mathbf{V}_r = \mathbf{T}_{c2} \mathbf{U}_{\mathbf{B}_{c3}}^T \mathbf{T}_{c2} \mathbf{V}_r. \quad (68)$$

- Tilt Motion:

$$\begin{cases} \mathbf{A}_3 \mathbf{V}_r = \mathbf{z}_r \dot{q}_{3_r} + \mathbf{B}_{13} \mathbf{U}_{\mathbf{A}_3}^T \mathbf{B}_{13} \mathbf{V}_r, \\ \mathbf{T}_{13} \mathbf{V}_r = \mathbf{A}_3 \mathbf{U}_{\mathbf{T}_{13}}^T \mathbf{A}_3 \mathbf{V}_r, \end{cases} \quad (69)$$

$$\begin{cases} \mathbf{C}_3 \mathbf{V}_r = \mathbf{z}_r \dot{q}_{13_r} + \mathbf{B}_{23} \mathbf{U}_{\mathbf{C}_3}^T \mathbf{B}_{23} \mathbf{V}_r, \\ \mathbf{D}_3 \mathbf{V}_r = \mathbf{x}_f \dot{x}_{3_r} + \mathbf{C}_3 \mathbf{U}_{\mathbf{D}_3}^T \mathbf{C}_3 \mathbf{V}_r, \\ \mathbf{T}_{23} \mathbf{V}_r = \mathbf{z}_r \dot{q}_{23_r} + \mathbf{D}_3 \mathbf{U}_{\mathbf{T}_{23}}^T \mathbf{D}_3 \mathbf{V}_r, \end{cases} \quad (70)$$

The quantities \dot{x}_{3_r} , \dot{q}_{3_r} , \dot{q}_{13_r} , and \dot{q}_{23_r} can be determined by substituting $\dot{\zeta}_{3_r}$, obtained from (63), into the set of Equations (39–44). Subsequently, the required linear/angular velocity vector at the base of the following component (i.e., the wrist) is computed as:

$$\mathbf{B}_4 \mathbf{V}_r = \mathbf{T}_{c3} \mathbf{U}_{\mathbf{B}_4}^T \mathbf{T}_{c3} \mathbf{V}_r. \quad (71)$$

- Wrist Motion:

$$\begin{cases} \mathbf{A}_4 \mathbf{V}_r = \mathbf{x}_r \dot{\zeta}_{4_r} + \mathbf{B}_4 \mathbf{U}_{\mathbf{A}_4}^T \mathbf{B}_4 \mathbf{V}_r, \\ \mathbf{C}_4 \mathbf{V}_r = \mathbf{z}_r \dot{\zeta}_{5_r} + \mathbf{A}_4 \mathbf{U}_{\mathbf{C}_4}^T \mathbf{A}_4 \mathbf{V}_r, \\ \mathbf{D}_4 \mathbf{V}_r = \mathbf{x}_r \dot{\zeta}_{6_r} + \mathbf{C}_4 \mathbf{U}_{\mathbf{D}_4}^T \mathbf{C}_4 \mathbf{V}_r, \\ \mathbf{T}_4 \mathbf{V}_r = \mathbf{D}_4 \mathbf{U}_{\mathbf{T}_4}^T \mathbf{D}_4 \mathbf{V}_r, \end{cases} \quad (72)$$

where $\dot{\zeta}_{4_r}$, $\dot{\zeta}_{5_r}$, and $\dot{\zeta}_{6_r}$ denote the required joint angular velocities associated with the wrist, and their values are directly determined from (63).

2) *Required Force/Moment Vectors*: Having derived the required linear/angular velocity vectors for each component, the corresponding force/moment vectors (\mathbf{F}_r^*) for all components can now be computed using (9). Accordingly, following the VDC methodology, the required force/moment vectors for each component are derived by substituting the corresponding required terms into the dynamic equations introduced in the modeling section (see Section III-A2).

- Wrist Motion:

For the wrist object, the required force/moment vectors are governed by the following equations:

$$\begin{cases} \mathbf{D}_4 \mathbf{F}_r = \mathbf{D}_4 \mathbf{F}_r^* + \mathbf{D}_4 \mathbf{U}_{\mathbf{T}_4}^T \mathbf{T}_4 \mathbf{F}_r, \\ \mathbf{C}_4 \mathbf{F}_r = \mathbf{C}_4 \mathbf{F}_r^* + \mathbf{C}_4 \mathbf{U}_{\mathbf{D}_4}^T \mathbf{D}_4 \mathbf{F}_r, \\ \mathbf{A}_4 \mathbf{F}_r = \mathbf{A}_4 \mathbf{F}_r^* + \mathbf{A}_4 \mathbf{U}_{\mathbf{C}_4}^T \mathbf{C}_4 \mathbf{F}_r, \\ \mathbf{B}_4 \mathbf{F}_r = \mathbf{B}_4 \mathbf{F}_r^* + \mathbf{B}_4 \mathbf{U}_{\mathbf{A}_4}^T \mathbf{A}_4 \mathbf{F}_r, \end{cases} \quad (73)$$

- Tilt Motion:

Now, by substituting the required force/moment vectors into (51) and (52), the following expressions are obtained:

$$\begin{aligned} \mathbf{B}_{c3} \mathbf{F}_r = & \mathbf{B}_{13} \mathbf{F}_r^* + \mathbf{B}_{13} \mathbf{U}_{\mathbf{A}_3}^T \mathbf{A}_3 \mathbf{F}_r^* + \mathbf{B}_{23} \mathbf{U}_{\mathbf{C}_3}^T \mathbf{C}_3 \mathbf{F}_r^* \\ & + \mathbf{B}_{23} \mathbf{U}_{\mathbf{C}_3}^T \mathbf{C}_3 \mathbf{U}_{\mathbf{D}_3}^T \mathbf{D}_3 \mathbf{F}_r^* + \mathbf{B}_{13} \mathbf{U}_{\mathbf{A}_3}^T \mathbf{A}_3 \mathbf{U}_{\mathbf{B}_4}^T \mathbf{B}_4 \mathbf{F}_r^*, \end{aligned} \quad (74)$$

$$\begin{aligned} f_{r3} = & \mathbf{x}_f^T \mathbf{D}_3 \mathbf{F}_r^* - \frac{\mathbf{z}_r^T (\mathbf{A}_3 \mathbf{F}_r^* + \mathbf{A}_3 \mathbf{U}_{\mathbf{B}_4}^T \mathbf{B}_4 \mathbf{F}_r^*)}{L_{13} \sin q_{23}} \\ & - \frac{\mathbf{z}_r^T (\mathbf{C}_3 \mathbf{F}_r^* + \mathbf{D}_3 \mathbf{F}_r^*) + \mathbf{y}_f^T (\mathbf{D}_3 \mathbf{F}_r^*) (x_3 + x_{03} - l_{c3})}{(x_3 + x_{03}) \tan q_{23}}. \end{aligned} \quad (75)$$

- Lift Motion:

For the lift motion, substituting the required force/moment vectors into (53) and (54) yields the following result:

$$\begin{aligned} \mathbf{B}_{c2} \mathbf{F}_r = & \mathbf{B}_{12} \mathbf{F}_r^* + \mathbf{B}_{12} \mathbf{U}_{\mathbf{A}_2}^T \mathbf{A}_2 \mathbf{F}_r^* + \mathbf{B}_{22} \mathbf{U}_{\mathbf{C}_2}^T \mathbf{C}_2 \mathbf{F}_r^* \\ & + \mathbf{B}_{22} \mathbf{U}_{\mathbf{C}_2}^T \mathbf{C}_2 \mathbf{U}_{\mathbf{D}_2}^T \mathbf{D}_2 \mathbf{F}_r^* + \mathbf{B}_{12} \mathbf{U}_{\mathbf{A}_2}^T \mathbf{A}_2 \mathbf{U}_{\mathbf{B}_3}^T \mathbf{B}_3 \mathbf{F}_r^*, \end{aligned} \quad (76)$$

$$f_{r2} = \mathbf{x}_f^T \mathbf{D}_2 \mathbf{F}_r^* - \frac{\mathbf{z}_\tau^T (\mathbf{A}_2 \mathbf{F}_r^* + \mathbf{A}_2 \mathbf{U}_{B_{c3}} \mathbf{B}_{c3} \mathbf{F}_r)}{L_{12} \sin q_{22}} - \frac{\mathbf{z}_\tau^T (\mathbf{C}_2 \mathbf{F}_r^* + \mathbf{D}_2 \mathbf{F}_r^*) + \mathbf{y}_f^T (\mathbf{D}_2 \mathbf{F}_r^*) (x_2 + x_{02} - l_{c2})}{(x_2 + x_{02}) \tan q_{22}}. \quad (77)$$

• Base Motion:

Finally, the required force/moment vector at the base of the manipulator, along with the corresponding required force at the base EMLA, are given by:

$$\mathbf{T}_1 \mathbf{F}_r = \mathbf{T}_1 \mathbf{F}_r^* + \mathbf{T}_1 \mathbf{U}_{B_{c2}} \mathbf{B}_{c2} \mathbf{F}_r, \quad (78)$$

$$f_{r1} = \frac{1}{r_B} \mathbf{y}_\tau^T (\mathbf{T}_1 \mathbf{F}_r). \quad (79)$$

B. Low-Level control

Given the required forces and velocities, the EMLAs must now produce the corresponding motions and forces. By integrating the surrogate-enhanced EMLA model introduced in Section III-B into the actuator control framework, the following low-level controller is designed for each EMLA to ensure the stability of the closed-loop system:

$$\begin{cases} v_{dr} = R_s i_d + L_d \frac{di_{dr}}{dt} - p \dot{\theta}_m \lambda_q + K_i (i_{dr} - i_d), \\ v_{qr} = R_s i_q + L_q \frac{di_{qr}}{dt} + p \dot{\theta}_m \lambda_d \\ \quad + K_f (F_{hyb_r} - F_{hyb}) + K_v (\dot{x}_r - \dot{x}). \end{cases} \quad (80)$$

Here, K_i , K_f , and K_v are positive control gains, while i_d and i_q denote the currents of the PMSM. The external force F_{hyb} is obtained from the surrogate-enhanced EMLA model described in (61), while F_{hyb_r} represents the required force for each EMLA, as derived in (75), (77), and (79). The term \dot{x} denotes the actual linear velocity, and \dot{x}_r is the corresponding required linear velocity for each EMLA. It is worth noting that the model-based terms in (80) serve to compensate for the dynamics of the actuator. Meanwhile, the error feedback terms are designed to regulate the tracking performance in current, force, and velocity simultaneously, ensuring stable closed-loop behavior.

The required current i_{dr} is calculated as follows:

$$\frac{d}{dt} i_{dr} = \frac{d}{dt} i_{dd} + \lambda_i (i_{dd} - i_d), \quad (81)$$

where i_{dd} is the desired current, and λ_i is a positive control gain. It is worth mentioning that setting $\frac{d}{dt} i_{dd} = i_{dd} = 0$ corresponds to the conventional strategy for efficient PMSM operation [64], [65].

The required current i_{qr} is computed from (61) when employing the EMLA dynamics, as outlined in Section II-B, as follows:

$$F_{hyb_r} = (1 - \alpha) \left(\frac{2\pi N_{\text{gear}}}{\rho} \right) \left[\frac{3}{2} p (\lambda_d i_{qr} - \lambda_q i_{dr}) - \left(J_m + \frac{M_{\text{act}}}{N_{\text{gear}} + \eta_f} \right) \ddot{\theta}_m - C_m \dot{\theta}_m - \tau_C \right] + \alpha \hat{F}_{\text{ext}}. \quad (82)$$

C. Stability Proof

As previously mentioned, the high-level controller at the manipulator level computes the required forces and velocities to control the rigid body subsystem (Section IV-A). Subsequently, the low-level controller at the actuator level is responsible for generating these required forces and velocities (Section IV-B). In this section, VPFs are used to establish the connections between the rigid body subsystems and the actuator subsystems.

Theorem 2: Consider the manipulator demonstrated in Fig. 1 that is decomposed into rigid body subsystems. The rigid body dynamics (6) under the rigid body local controller (9) with the adaptation laws (14) is virtually stable in the sense of Definition 3.

Proof: Let the non-negative accompanying function for the rigid body part be chosen in the sense of Definition 2, as follows:

$$\begin{aligned} \nu_1 = & \sum_{A \in \Upsilon} \frac{1}{2} (\mathbf{A} \mathbf{V}_r - \mathbf{A} \mathbf{V})^T \mathbf{M}_A (\mathbf{A} \mathbf{V}_r - \mathbf{A} \mathbf{V}) \\ & + \sum_{A \in \Upsilon} \gamma \mathcal{D}_F(\mathcal{L}_A \| \hat{\mathcal{L}}_A). \end{aligned} \quad (83)$$

where $\mathcal{D}_F(\mathcal{L}_A \| \hat{\mathcal{L}}_A)$ is in the sense of (12) and where $A \in \Upsilon$ and $\Upsilon = \{T_1, A_i, B_{c_i}, C_i, D_i\}$ for $i = 2, 3, 4$. Taking the time derivative of ν_1 and following the procedure explained in [14, Appendix A] yield the follows:

$$\dot{\nu}_1 \leq - \sum_{A \in \Upsilon} (\mathbf{A} \mathbf{V}_r - \mathbf{A} \mathbf{V})^T \mathbf{K}_A (\mathbf{A} \mathbf{V}_r - \mathbf{A} \mathbf{V}) + VPFs \quad (84)$$

with VPFs denoting the sum of driving and driven cutting points in the sense of Definition 1. It can be seen from (84) that the rigid body subsystem is virtually stable in the sense of Definition 3.

Theorem 3: The actuator dynamics, driven by the required EMLA forces (75), (77), and (79), and controlled by the low-level controller (80), are virtually stable according to Definition 3.

Proof: To begin, we consider the actual forces generated by each EMLA derived from (61), based on the EMLA dynamics described in Section II-B, and we proceed to design the required forces as follows:

$$\begin{cases} F_{hyb} = (1 - \alpha) \left(\frac{2\pi N_{\text{gear}}}{\rho} \right) \left[\frac{3}{2} p (\lambda_d i_q - \lambda_q i_d) - \left(J_m + \frac{M_{\text{act}}}{N_{\text{gear}} + \eta_f} \right) \ddot{\theta}_m - C_m \dot{\theta}_m - \tau_C \right] + \alpha \hat{F}_{\text{ext}}, \\ F_{hyb_r} = (1 - \alpha) \left(\frac{2\pi N_{\text{gear}}}{\rho} \right) \left[\frac{3}{2} p (\lambda_d i_{qr} - \lambda_q i_{dr}) - \left(J_m + \frac{M_{\text{act}}}{N_{\text{gear}} + \eta_f} \right) \ddot{\theta}_m - C_m \dot{\theta}_m - \tau_C \right] + \alpha \hat{F}_{\text{ext}}. \end{cases} \quad (85)$$

By subtracting these equations, the force error for each EMLA can be computed as follows:

$$\begin{aligned} F_{\text{hyb}_r} - F_{\text{hyb}} &= (1 - \alpha) \left(\frac{2\pi N_{\text{gear}}}{\rho} \right) \left(\frac{3}{2}p \right) [\tau_{er} - \tau_e] \\ &= (1 - \alpha) \left(\frac{2\pi N_{\text{gear}}}{\rho} \right) \left(\frac{3}{2}p \right) [\lambda_d(i_{qr} - i_q) - \lambda_q(i_{dr} - i_d)] \\ &= \beta_1(i_{qr} - i_q) - \beta_2(i_{dr} - i_d), \end{aligned} \quad (86)$$

where β_1 and β_2 are introduced to encapsulate system parameters and simplify the equation. Differentiating (86), substituting $\frac{di_{dr}}{dt}$ and $\frac{di_{qr}}{dt}$ from (80) and $\frac{di_d}{dt}$ and $\frac{di_q}{dt}$ from (17), and using $v_{dr} = v_d$ and $v_{qr} = v_q$, yields:

$$\begin{aligned} \frac{d}{dt}(F_{\text{hyb}_r} - F_{\text{hyb}}) &= \frac{\beta_1}{L_q} [-K_f(F_{\text{hyb}_r} - F_{\text{hyb}}) - K_v(\dot{x}_r - \dot{x})] \\ &\quad + \frac{\beta_2}{L_d} [K_i(i_{dr} - i_d)]. \end{aligned} \quad (87)$$

Now, consider the non-negative accompanying function v_{a_j} for each EMLA ($j = 1, 2, 3$) as follows:

$$v_{a_j} = \frac{K_{1j}}{2}(F_{\text{hyb}_{rj}} - F_{\text{hyb}_j})^2 + \frac{K_{2j}}{2}(i_{drj} - i_{dj})^2. \quad (88)$$

Differentiating this equation, in conjunction with using (80) and (87), yields:

$$\begin{aligned} \dot{v}_{a_j} &= K_{1j}(F_{\text{hyb}_{rj}} - F_{\text{hyb}_j}) \frac{d}{dt}(F_{\text{hyb}_{rj}} - F_{\text{hyb}_j}) \\ &\quad + K_{2j}(i_{drj} - i_{dj}) \frac{d}{dt}(i_{drj} - i_{dj}) \\ &= K_{1j}(F_{\text{hyb}_{rj}} - F_{\text{hyb}_j}) \left(\frac{\beta_{1j}}{L_{qj}} [-K_{fj}(F_{\text{hyb}_{rj}} - F_{\text{hyb}_j}) \right. \\ &\quad \left. - K_{vj}(\dot{x}_{rj} - \dot{x}_j)] + \frac{\beta_{2j}}{L_{dj}} [K_{ij}(i_{drj} - i_{dj})] \right) \\ &\quad + \frac{K_{2j}}{L_{dj}}(i_{drj} - i_{dj}) \left(-K_{ij}(i_{drj} - i_{dj}) \right) \\ &= -\frac{K_{1j}\beta_{1j}K_{fj}}{L_{qj}}(F_{\text{hyb}_{rj}} - F_{\text{hyb}_j})^2 \\ &\quad - \frac{K_{1j}\beta_{1j}K_{vj}}{L_{qj}}(F_{\text{hyb}_{rj}} - F_{\text{hyb}_j})(\dot{x}_{rj} - \dot{x}_j) \\ &\quad + \frac{K_{1j}\beta_{2j}K_{ij}}{L_{dj}}(F_{\text{hyb}_{rj}} - F_{\text{hyb}_j})(i_{drj} - i_{dj}) \\ &\quad - \frac{K_{2j}K_{ij}}{L_{dj}}(i_{drj} - i_{dj})^2. \end{aligned} \quad (89)$$

Now, by applying Young's inequality to the term $(F_{\text{hyb}_{rj}} -$

$F_{\text{hyb}_j})(i_{drj} - i_{dj})$, we obtain:

$$\begin{aligned} \dot{v}_{a_j} &\leq -\frac{K_{1j}\beta_{1j}K_{fj}}{L_{qj}}(F_{\text{hyb}_{rj}} - F_{\text{hyb}_j})^2 \\ &\quad - \frac{K_{1j}\beta_{1j}K_{vj}}{L_{qj}}(F_{\text{hyb}_{rj}} - F_{\text{hyb}_j})(\dot{x}_{rj} - \dot{x}_j) \\ &\quad + \frac{K_{1j}\beta_{2j}K_{ij}}{2L_{dj}} [(F_{\text{hyb}_{rj}} - F_{\text{hyb}_j})^2 + (i_{drj} - i_{dj})^2] \\ &\quad - \frac{K_{2j}K_{ij}}{L_{dj}}(i_{drj} - i_{dj})^2 \\ &= -K_{1j} \left(\frac{\beta_{1j}K_{fj}}{L_{qj}} - \frac{\beta_{2j}K_{ij}}{2L_{dj}} \right) (F_{\text{hyb}_{rj}} - F_{\text{hyb}_j})^2 \\ &\quad - \frac{K_{ij}}{L_{dj}} \left(K_{2j} - \frac{K_{1j}\beta_{2j}}{2} \right) (i_{drj} - i_{dj})^2 \\ &\quad - \frac{K_{1j}\beta_{1j}K_{vj}}{L_{qj}}(F_{\text{hyb}_{rj}} - F_{\text{hyb}_j})(\dot{x}_{rj} - \dot{x}_j). \end{aligned} \quad (90)$$

Therefore, if the following conditions are satisfied:

$$\begin{cases} \frac{\beta_{1j}K_{fj}}{L_{qj}} \geq \frac{\beta_{2j}K_{ij}}{2L_{dj}}, \\ K_{2j} \geq \frac{K_{1j}\beta_{2j}}{2}, \\ K_{1j} = \frac{L_{qj}}{\beta_{1j}K_{vj}}, \end{cases} \quad (91)$$

all the actuators are virtually stable according to Definition 3:

$$\begin{aligned} \dot{v}_{a_j} &\leq -K_{1j} \left(\frac{\beta_{1j}K_{fj}}{L_{qj}} - \frac{\beta_{2j}K_{ij}}{2L_{dj}} \right) (F_{\text{hyb}_{rj}} - F_{\text{hyb}_j})^2 \\ &\quad - \frac{K_{ij}}{L_{dj}} \left(K_{2j} - \frac{K_{1j}\beta_{2j}}{2} \right) (i_{drj} - i_{dj})^2 - VPF_j. \end{aligned} \quad (92)$$

Theorem 4: The entire system, decomposed into rigid body and actuator subsystems, is stable under the low-level control law (80); high-level control laws (75), (77), and (79); and adaptation law (14).

Proof: Define the non-negative accompanying function as below:

$$\nu = \nu_1 + \sum_{j=1}^3 \nu_{a_j}. \quad (93)$$

By taking the time derivative of (93), substituting from (84) and (92), and applying the conditions in (91), one obtains:

$$\begin{aligned} \dot{\nu} &\leq -\sum_{A \in \Upsilon} (\mathbf{A}\mathbf{V}_r - \mathbf{A}\mathbf{V})^T \mathbf{K}_A (\mathbf{A}\mathbf{V}_r - \mathbf{A}\mathbf{V}) \\ &\quad - \sum_{j=1}^3 \left[K_{1j} \left(\frac{\beta_{1j}K_{fj}}{L_{qj}} - \frac{\beta_{2j}K_{ij}}{2L_{dj}} \right) (F_{\text{hyb}_{rj}} - F_{\text{hyb}_j})^2 \right. \\ &\quad \left. + \frac{K_{ij}}{L_{dj}} \left(K_{2j} - \frac{K_{1j}\beta_{2j}}{2} \right) (i_{drj} - i_{dj})^2 \right], \end{aligned} \quad (94)$$

demonstrating the stability of the system under the designed controllers.

V. RESULTS AND DISCUSSION

For a rigorous evaluation of the performance of the proposed adaptive modular controller for the all-electric HDRM, it is essential to assess its behavior under various motion scenarios using standardized trajectories. In this study, two representative trajectories are employed: (1) the cubic trajectory, a widely recognized three-dimensional path used for benchmarking industrial robot accuracy and repeatability, and (2) a planar triangular trajectory designed to evaluate motion control performance in two-dimensional constrained environments. Both trajectories are schematically illustrated in Fig. 8.

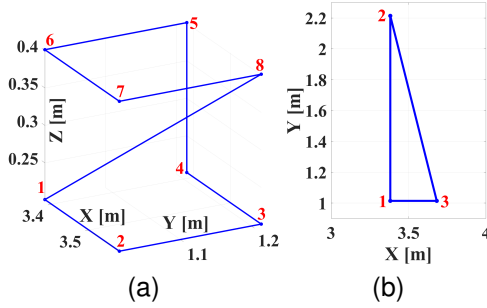


Fig. 8. Schematic view of the trajectories. a) Cubic trajectory with 20 cm length. b) Planar triangular trajectory.

A. Simulation Results

In this section, the simulation results of the proposed adaptive modular controller are compared with two baseline controllers: (1) a modular controller, which corresponds to the proposed architecture without the adaptive component, and (2) a PD controller, obtained by removing both the adaptive module and the model-based dynamic compensation, retaining only proportional-derivative feedback control.

Fig. 9 illustrates the Cartesian tracking performance in the end effector for the three controllers, adaptive modular, modular and PD, while performing the cubic trajectory shown in Figure 8a. This standardized 3D motion path provides a comprehensive assessment of each controller's ability to handle complex spatial trajectories. The tracking results of the end-effector in Cartesian space for the three controllers during execution of the triangular trajectory (illustrated in Fig. 8b) are presented in Fig. 10. It can be observed that the proposed adaptive modular controller demonstrates superior tracking performance compared to the other controllers when following the triangular trajectory. Specifically, it achieves significantly lower Cartesian tracking errors throughout the motion, indicating its effectiveness in compensating for dynamic uncertainties and improving end-effector tracking accuracy.

To assess the robustness of the proposed controller against parametric uncertainties, the root mean squared error (RMSE) is employed as a performance metric. The controller's tracking performance is evaluated under +40%, +20%, nominal, -20%, and -40% variations in system parameters while following the two previously described trajectories. The corresponding results are presented in Table I.

TABLE I
RMSE OF THE PROPOSED CONTROLLER UNDER PARAMETRIC UNCERTAINTIES FOR TWO TRAJECTORIES.

Uncertainty	Cubic Trajectory	Triangular Trajectory
+40 %	0.0024 m	0.0042 m
+20 %	0.0019 m	0.0035 m
0 % (Nominal)	0.0015 m	0.0029 m
-20 %	0.0029 m	0.0050 m
-40 %	0.0036 m	0.0060 m

As observed in Table I, the RMSE remains consistently low across all levels of uncertainty, with only a gradual increase as the deviation from nominal parameters grows. This behavior demonstrates the controller's ability to maintain accurate trajectory tracking despite significant parametric variations.

B. Experimental Results

For an experimental validation of the performance of the proposed adaptive modular controller for the all-electric HDRM, a series of motion-tracking experiments was carried out using a dedicated EMLA-driven testbed. The primary objective was to assess the trajectory tracking fidelity and control robustness under realistic operating conditions.

The experimental platform consists of a three-phase, 380/480V, 8-pole Nidec PMSM rated at 11.6 kW. This motor is coupled to a reduction gearbox and a screw mechanism, forming a complete EMLA. The EMLA system is mechanically connected to another actuator that acts as an external load emulator, capable of generating dynamic and time-varying force profiles via an electrohydraulic human-machine interface (HMI). The load emulation closely replicates the operational disturbances typically encountered in the lift and tilt joints of an HDRM. Meanwhile, a Unidrive M700 servo controller governs the PMSM operation through a subsystem-based control interface [66]–[68]. The setup features real-time signal acquisition and actuation feedback, coordinated via an EtherCAT communication network, enabling synchronized voltage control, force feedback, and trajectory monitoring with high temporal resolution. The same benchmark trajectories used in the simulation section were employed for experimental validation: the cubic trajectory for assessing 3D tracking accuracy, and a planar triangular trajectory for evaluating controller performance in constrained planar motion.

Fig. 11 shows the experimental testbed used for evaluating the lift and tilt actuators under these benchmark trajectories, while the results for the lift actuator tracking the cubic trajectory are illustrated in Fig. 12, followed by the corresponding results for the tilt actuator in Fig. 13. These figures present a comparison between the desired reference trajectories and the experimentally recorded force, velocity, and position responses. To evaluate the performance further under 2D constraints, the planar triangular trajectory was applied to both joints. The resulting performance of the lift and tilt actuators under this trajectory is shown in Fig. 14 and Fig. 15, respectively. In all cases, the proposed modular adaptive controller demonstrates accurate trajectory tracking and effective disturbance rejection, even in the presence of realistic dynamic loads.

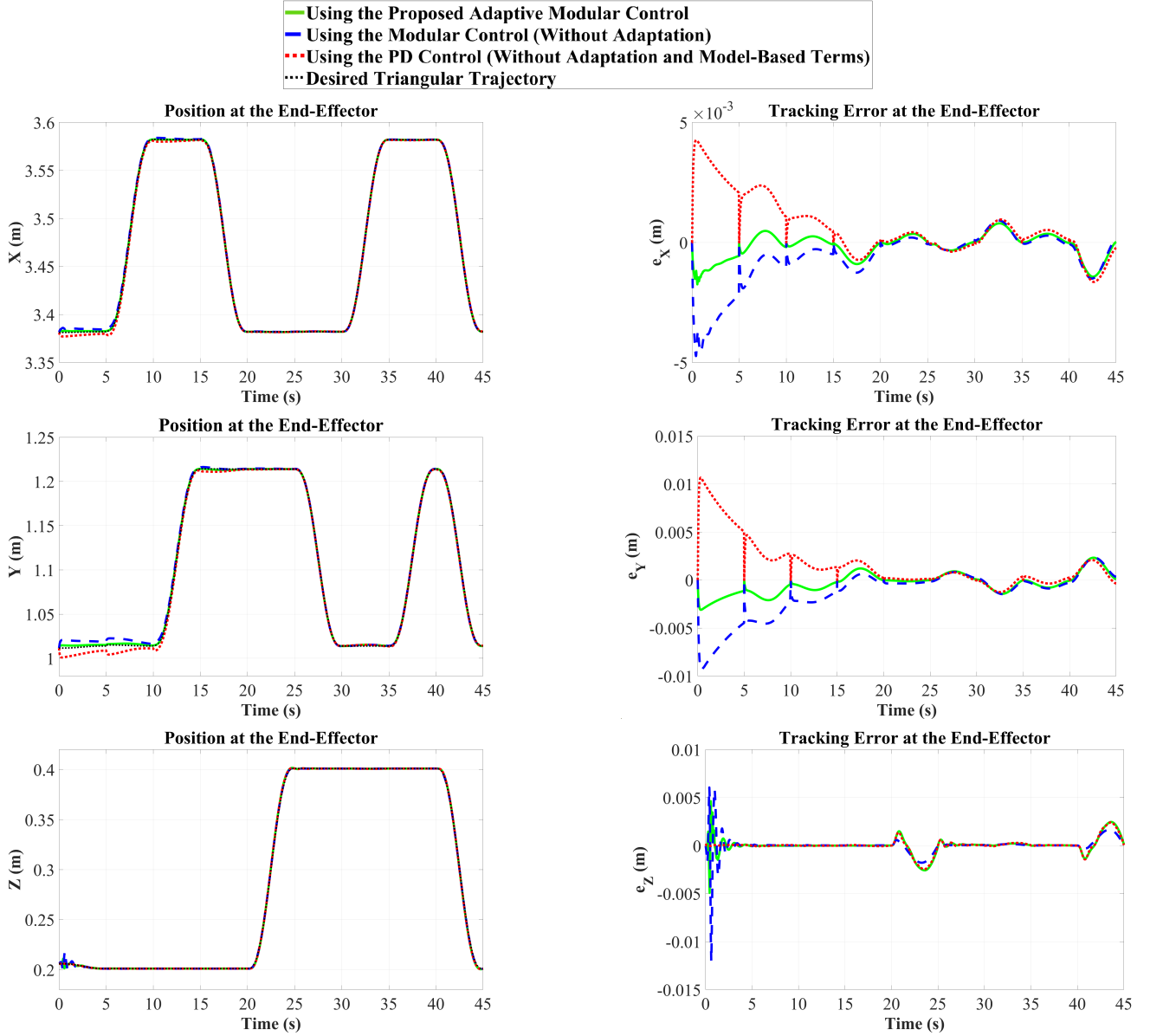


Fig. 9. Performance comparison of controllers using the cubic trajectory.

VI. CONCLUSION

This paper has presented a unified system-level modeling and control methodology for a 6-DoF HDRM, actuated exclusively by EMLAs. A hybrid actuator model was constructed by involving a physics-based description of the electromechanical dynamics and data-driven surrogate trained on a dedicated 1-DoF testbed. This surrogate-enhanced model was embedded in an extended VDC framework augmented by a natural adaptation law to guarantee robustness against parametric uncertainties. The derived analytical manipulator model underpins a hierarchical control scheme that maps high-level force and velocity objectives to low-level voltage and current commands.

The complete architecture was evaluated in a multi-domain simulation with both the cubic benchmark and a custom planar triangular trajectory. In the simulation, the proposed adaptive

modular controller achieved sub-centimeter Cartesian tracking accuracy, while experimental validation of the same 1-DoF platform under realistic load emulation confirmed a simulated performance and showcased precise motion tracking under dynamic force variations. A Lyapunov-based stability proof verified that the combined rigid-body VDC subsystems and low-level EMLA controllers yield an asymptotically stable closed-loop system.

These results illustrate that a hybrid modeling and VDC architecture can deliver high-precision, robust control of a fully electric HDRM while remaining modular and real-time implementable, positioning a fully electric HDRM as a viable alternative to traditional hydraulic systems in MWM applications. Future work will extend hardware-in-the-loop validation to the full 6-DoF manipulator, enable online adaptation during operation, and integrate holistic energy and thermal management to support sustained field deployments.

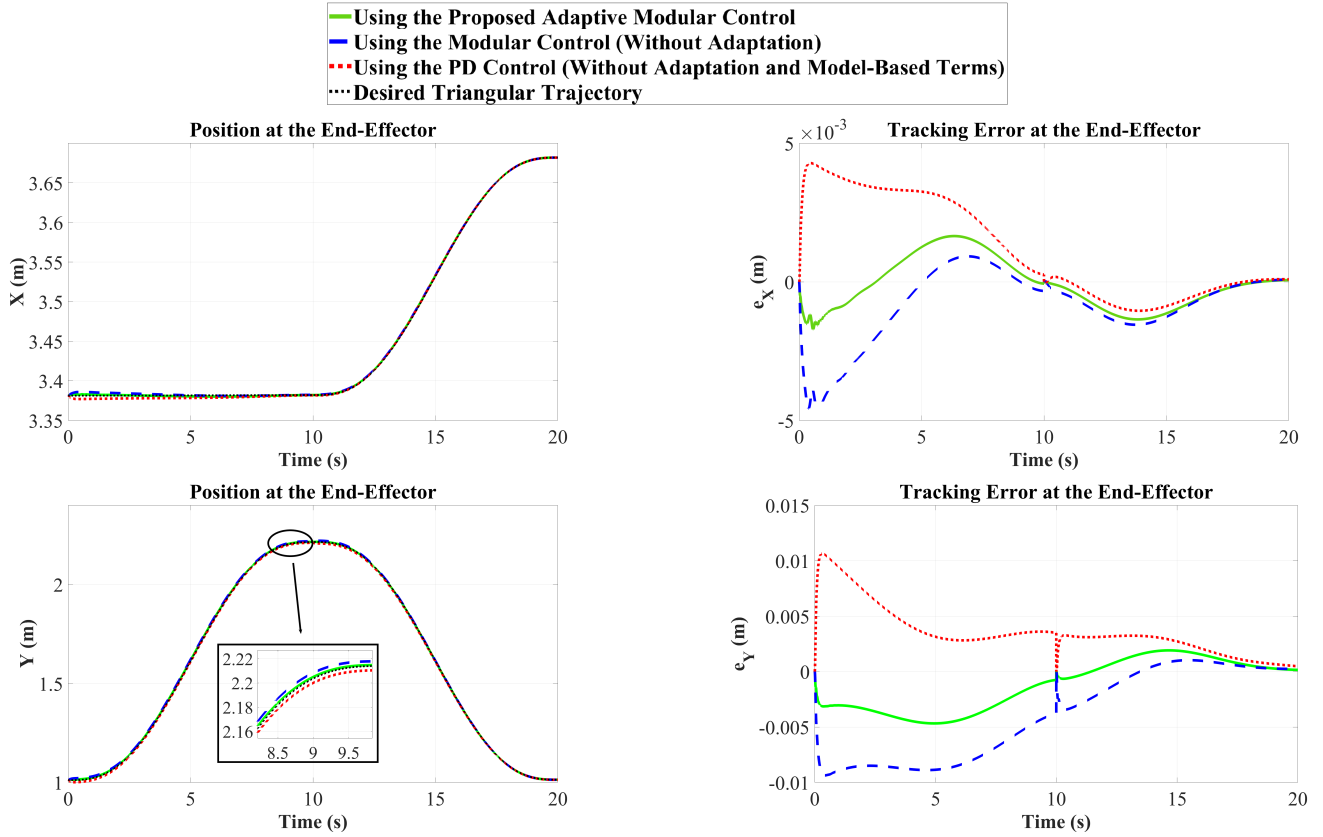


Fig. 10. Performance comparison of controllers using the planar triangular trajectory.

REFERENCES

- [1] X. Wang, D. Wang, M. Du, K. Song, Y. Ni, and Y. Li, "A two-layer trajectory tracking control scheme of manipulator based on elm-smc for autonomous robotic vehicle," *IEEE Transactions on Automation Science and Engineering*, 2023.
- [2] F. Ostyn, B. Vanderborcht, and G. Crevecoeur, "Improving the collision tolerance of high-speed industrial robots via impact-aware path planning and series clutched actuation," *IEEE Transactions on Robotics*, 2024.
- [3] A. H. Barjini, S. Yaqubi, S. M. Tahamipour-Z, and J. Mattila, "Deep learning-based deflection correction and end-point control of heavy-duty vertical single-link flexible manipulators," in *2024 IEEE International Conference on Robotics and Biomimetics (ROBIO)*. IEEE, 2024, pp. 905–912.
- [4] J. Mattila, J. Koivumäki, D. G. Caldwell, and C. Semini, "A survey on control of hydraulic robotic manipulators with projection to future trends," *IEEE/ASME Transactions on Mechatronics*, vol. 22, no. 2, pp. 669–680, 2017.
- [5] A. Billard and D. Kragic, "Trends and challenges in robot manipulation," *Science*, vol. 364, no. 6446, p. eaat8414, 2019.
- [6] M. Hejrati and J. Mattila, "Impact-resilient orchestrated robust controller for heavy-duty hydraulic manipulators," *IEEE/ASME Transactions on Mechatronics*, 2025.
- [7] A. Mohanty and B. Yao, "Integrated direct/indirect adaptive robust control of hydraulic manipulators with valve deadband," *IEEE/ASME Transactions on Mechatronics*, vol. 16, no. 4, pp. 707–715, 2010.
- [8] T. Mononen, M. M. Aref, and J. Mattila, "Nonlinear model predictive control of a heavy-duty hydraulic bulldozer blade," in *2019 IEEE International Conference on Cybernetics and Intelligent Systems (CIS) and IEEE Conference on Robotics, Automation and Mechatronics (RAM)*. IEEE, 2019, pp. 565–570.
- [9] X. Liang, Z. Yao, W. Deng, and J. Yao, "Adaptive neural network finite-time tracking control for uncertain hydraulic manipulators," *IEEE/ASME Transactions on Mechatronics*, 2024.
- [10] Z. Yao, F. Xu, G.-P. Jiang, and J. Yao, "Data-driven control of hydraulic manipulators by reinforcement learning," *IEEE/ASME Transactions on Mechatronics*, vol. 29, no. 4, pp. 2673–2684, 2023.
- [11] H. V. A. Truong, S. Nam, S. Kim, Y. Kim, and W. K. Chung, "Backstepping-sliding-mode-based neural network control for electro-hydraulic actuator subject to completely unknown system dynamics," *IEEE Transactions on Automation Science and Engineering*, vol. 21, no. 4, pp. 6202–6216, 2023.
- [12] W.-H. Zhu, *Virtual decomposition control: toward hyper degrees of freedom robots*. Springer Science & Business Media, 2010, vol. 60.
- [13] J. Koivumäki and J. Mattila, "Stability-guaranteed force-sensorless contact force/motion control of heavy-duty hydraulic manipulators," *IEEE Transactions on Robotics*, vol. 31, no. 4, pp. 918–935, 2015.
- [14] M. Hejrati and J. Mattila, "Orchestrated robust controller for precision control of heavy-duty hydraulic manipulators," *IEEE Transactions on Automation Science and Engineering*, 2025.
- [15] J. Koivumäki and J. Mattila, "High performance nonlinear motion/force controller design for redundant hydraulic construction crane automation," *Automation in construction*, vol. 51, pp. 59–77, 2015.
- [16] J. Koivumäki, W.-H. Zhu, and J. Mattila, "Energy-efficient and high-precision control of hydraulic robots," *Control Engineering Practice*, vol. 85, pp. 176–193, 2019.
- [17] G. R. Petrović and J. Mattila, "Mathematical modelling and virtual decomposition control of heavy-duty parallel–serial hydraulic manipulators," *Mechanism and Machine Theory*, vol. 170, p. 104680, 2022.
- [18] N. T. Dat, C. Van Kien, and H. P. H. Anh, "Advanced adaptive neural sliding mode control applied in pmsm driving system," *Electrical Engineering*, vol. 105, no. 5, pp. 3255–3262, 2023.
- [19] K. Zhao, W. Liu, T. Yin, R. Zhou, and W. Dai, "Model-free sliding mode control for pmsm drive system based on ultra-local model," *Energy Engineering: Journal of the Association of Energy Engineers*, vol. 119, no. 2, p. 767, 2022.
- [20] S. Niu, Y. Luo, W. Fu, and X. Zhang, "Robust model predictive control for a three-phase pmsm motor with improved control precision," *IEEE Transactions on Industrial Electronics*, vol. 68, no. 1, pp. 838–849, 2020.
- [21] P. Sorknæs, R. M. Johannsen, A. D. Korberg, T. B. Nielsen, U. R. Petersen, and B. V. Mathiesen, "Electrification of the industrial sector in 100% renewable energy scenarios," *Energy*, vol. 254, p. 124339, 2022.
- [22] S. Bellocchi, M. Manno, M. Noussan, M. G. Prina, and M. Vellini, "Electrification of transport and residential heating sectors in support of

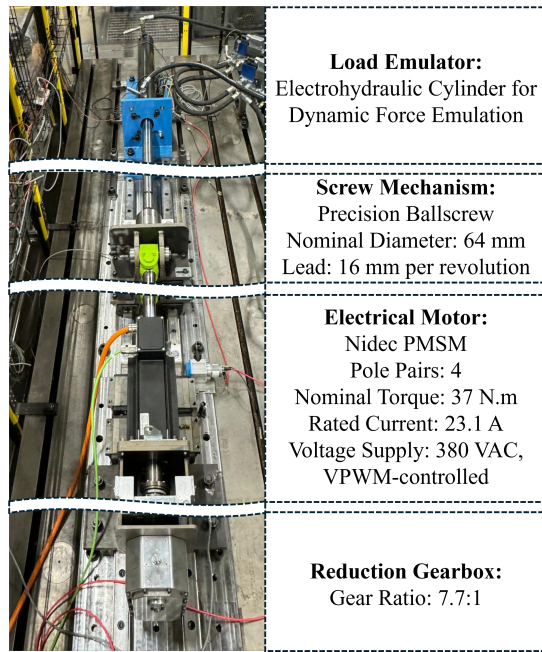


Fig. 11. Experimental setup used to validate the proposed control strategy. The testbed includes the Nidec PMSM, a reduction gearbox, and a high-precision screw forming the EMLA, as well as electrohydraulic cylinder as the load emulator.

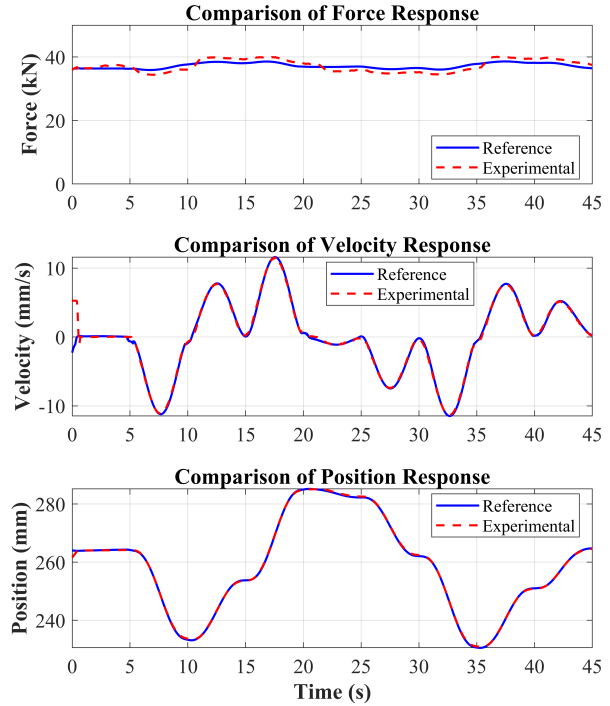


Fig. 12. Experimental tracking results for the lift actuator under the cubic trajectory, illustrating tracking accuracy under three-dimensional motion.

- renewable penetration: Scenarios for the Italian energy system,” *Energy*, vol. 196, p. 117062, 2020.
- [23] N. Gadiyar, G. Bohach, M. M. Nahin, J. Van de Ven, and E. L. Severson, “Development of an integrated electro-hydraulic machine to electrify off-highway vehicles,” *IEEE Transactions on Industry Applications*, vol. 58, no. 5, pp. 6163–6174, 2022.
- [24] United Nations Framework Convention on Climate Change, “The Paris Agreement,” <https://unfccc.int/process-and-meetings/the-paris-agreement/the-paris-agreement>, 2015, adopted at COP21, Paris, December 2015.
- [25] European Parliament and Council, “Regulation (EU) 2023/851: CO₂ emission performance standards for cars and vans – zero emissions by 2035,” <https://eur-lex.europa.eu/legal-content/EN/TXT/?uri=CELEX:32023R0851>, 2023, official Journal of the European Union, L 111/1, 25 April 2023.
- [26] IEA Advanced Motor Fuels Technology Collaboration Programme, “Fuel options for off-road machines: Final report, annex 50,” https://www.iea-amf.org/content/projects/map_projects/50, International Energy Agency (IEA), Tech. Rep., 2023, aMF Annex 50 Final Report, May 2023.
- [27] A. M. EL-Refaie, “Electrical machines for traction and propulsion applications,” *Transportation Electrification: Breakthroughs in Electrified Vehicles, Aircraft, Rolling Stock, and Watercraft*, pp. 1–26, 2022.
- [28] N. Gadiyar, J. Van de Ven, and E. L. Severson, “Evaluation of torque-density electric machine technology for off-highway vehicle electrification,” *IEEE Transactions on Industry Applications*, vol. 60, no. 2, pp. 3062–3074, 2024.
- [29] M. d. F. Ramos, D. A. d. L. Brandao, D. P. Galo, B. d. J. Cardoso Filho, I. A. Pires, and T. A. Maia, “A study on the performance of the electrification of hydraulic implements in a compact non-road mobile machine: A case applied to a backhoe loader,” *World Electric Vehicle Journal*, vol. 15, no. 4, p. 127, 2024.
- [30] M. Bahari, A. Paz, A. S. Habib, and J. Mattila, “Performance evaluation of an electromechanical linear actuator with optimal trajectories,” in *2023 IEEE 97th Vehicular Technology Conference (VTC2023-Spring)*. IEEE, 2023, pp. 1–7.
- [31] S. Qu, F. Zappaterra, A. Vacca, and E. Busquets, “An electrified boom actuation system with energy regeneration capability driven by a novel electro-hydraulic unit,” *Energy Conversion and Management*, vol. 293, p. 117443, 2023.
- [32] A. Paz, M. Bahari, and J. Mattila, “Energy-cautious designation of kinematic parameters for a sustainable parallel-serial heavy-duty manipulator driven by electromechanical linear actuator,” in *2024 IEEE 100th Vehicular Technology Conference (VTC2024-Fall)*. IEEE, 2024, pp. 1–7.
- [33] R. Alipour-Sarabi, Z. Nasiri-Gheidari, F. Tootoonchian, and H. Oraee, “Performance analysis of concentrated wound-rotor resolver for its applications in high pole number permanent magnet motors,” *IEEE Sensors Journal*, vol. 17, no. 23, pp. 7877–7885, 2017.
- [34] S. Li, Y. Xu, W. Zhang, and J. Zou, “Robust deadbeat predictive direct speed control for pmsm with dual second-order sliding-mode disturbance observers and sensitivity analysis,” *IEEE Transactions on Power Electronics*, vol. 38, no. 7, pp. 8310–8326, 2023.
- [35] F. Tootoonchian and Z. Nasiri-Gheidari, “Cogging force mitigation techniques in a modular linear permanent magnet motor,” *IET Electric Power Applications*, vol. 10, no. 7, pp. 667–674, 2016.
- [36] M. Bahari, A. Paz, M. H. Shahna, P. Mustalahti, and J. Mattila, “System-level efficient performance of emla-driven heavy-duty manipulators via bilevel optimization framework with a leader-follower scenario,” *IEEE Transactions on Automation Science and Engineering*, 2025.
- [37] J. Chen, A. Behal, Z. Li, and C. Li, “Active battery cell balancing by real-time model predictive control for extending electric vehicle driving range,” *IEEE Transactions on Automation Science and Engineering*, vol. 21, no. 3, pp. 4003–4015, 2024.
- [38] J. Zhai, Y. Qin, and H. Cui, “Adaptive fault-tolerant tracking control for nonlinear systems with unknown actuator and multiple sensor faults,” *IEEE Transactions on Automation Science and Engineering*, 2025.
- [39] H. Saneie, Z. Nasiri-Gheidari, and F. Tootoonchian, “Design and prototyping of a multi-turn sinusoidal air-gap length resolver,” *IEEE Transactions on Energy Conversion*, vol. 35, no. 1, pp. 271–278, 2020.
- [40] M. Bahari, A. Davoodi, H. Saneie, F. Tootoonchian, and Z. Nasiri-Gheidari, “A new variable reluctance pm-resolver,” *IEEE Sensors Journal*, vol. 20, no. 1, pp. 135–142, 2020.
- [41] M. Khajepour, F. Zare, and Z. Nasiri-Gheidari, “Reliability analysis of two resolver configurations under faulty conditions in 2dof system,” *IEEE Transactions on Instrumentation and Measurement*, vol. 72, pp. 1–8, 2023.
- [42] Bobcat Company, “Bobcat T7X: World’s First All-Electric Compact Track Loader,” Press Release, CES 2022, 2022, accessed: 2025-06-02. [Online]. Available: <https://www.bobcat.com/na/en/news/press-releases/2022/bobcat-launches-all-electric-compact-track-loader-t7x>

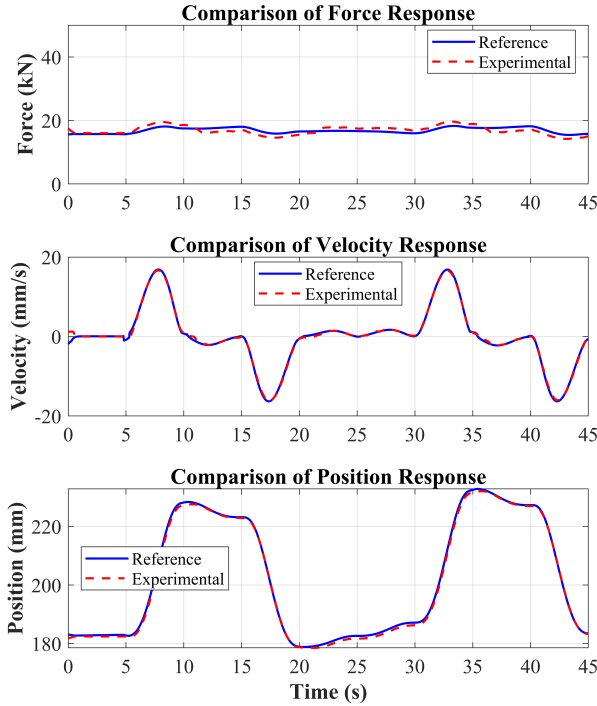


Fig. 13. Experimental tracking results for the tilt actuator under the cubic trajectory, illustrating tracking accuracy under 3D motion.

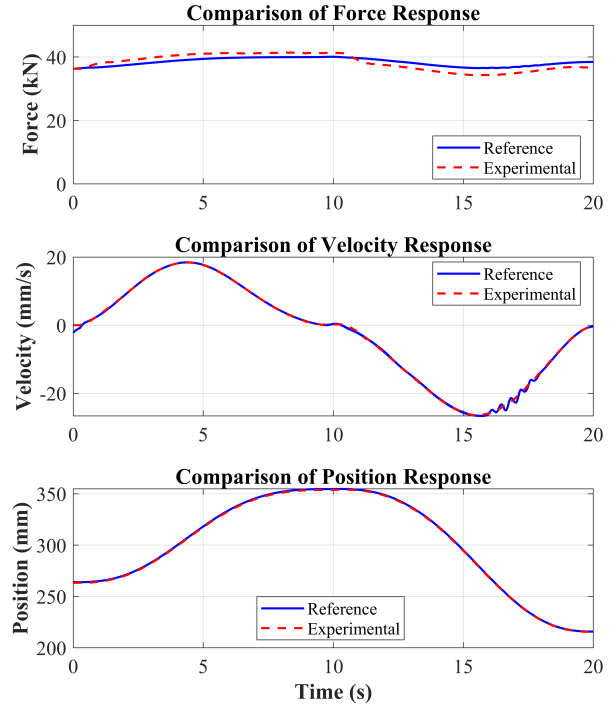


Fig. 14. Experimental tracking results for the lift actuator under the planar triangular trajectory, illustrating performance under two-dimensional constrained motion.

- [43] Volvo Construction Equipment, "Volvo Construction Equipment Unveils Its First Mid-Size Electric Wheeled Excavator Concept," Press Release, Jan. 2021, accessed: 2025-06-02.
- [44] D. Beltrami, P. Iora, L. Tribioli, and S. Uberti, "Electrification of compact off-highway vehicles—overview of the current state of the art and trends," *Energies*, vol. 14, no. 17, p. 5565, 2021.
- [45] K. Pate, F. El Breidi, T. Salem, and J. Lumkes, "Industry perspectives on electrifying heavy equipment: Trends, challenges, and opportunities," *Energies*, vol. 18, no. 11, p. 2806, 2025.
- [46] M. H. Shahna, M. Bahari, and J. Mattila, "Robustness-guaranteed observer-based control strategy with modularity for cleantech emla-driven heavy-duty robotic manipulator," *IEEE Transactions on Automation Science and Engineering*, 2024.
- [47] M. Al Saaideh, A. M. Boker, and M. Al Janaideh, "Output feedback with feedforward robust control for motion systems driven by nonlinear position-dependent actuators," *IEEE Transactions on Automation Science and Engineering*, 2024.
- [48] L. Liu, S. Leonhardt, C. Ngo, and B. J. Misgeld, "Impedance-controlled variable stiffness actuator for lower limb robot applications," *IEEE Transactions on Automation Science and Engineering*, vol. 17, no. 2, pp. 991–1004, 2019.
- [49] L. Ma, Z. Wang, H. Zhang, and Q. Wang, "Adaptive neural network constrained fault tolerant control for nonlinear systems with actuator failures and saturation," *IEEE Transactions on Automation Science and Engineering*, 2024.
- [50] M. Bahari, A. Paz, and J. Mattila, "System-level performance metrics sensitivity of an electrified heavy-duty mobile manipulator," in *2024 IEEE 100th Vehicular Technology Conference (VTC2024-Fall)*. IEEE, 2024, pp. 1–5.
- [51] H. Xing, Y. Xu, L. Ding, J. Chen, H. Gao, and M. Tavakoli, "Trajectory tracking control of wheeled mobile manipulators with joint flexibility via virtual decomposition approach," *IEEE Transactions on Automation Science and Engineering*, vol. 22, pp. 11 808–11 825, 2025.
- [52] X. Liang, Y. Wang, H. Yu, Z. Zhang, J. Han, and Y. Fang, "Observer-based nonlinear control for dual-arm aerial manipulator systems suffering from uncertain center of mass," *IEEE Transactions on Automation Science and Engineering*, vol. 22, pp. 1984–1995, 2025.
- [53] E. Kang, H. Qiao, Z. Chen, and J. Gao, "Tracking of uncertain robotic manipulators using event-triggered model predictive control with learning terminal cost," *IEEE Transactions on Automation Science and Engineering*, vol. 19, no. 4, pp. 2801–2815, 2022.
- [54] M. Hejrati and J. Mattila, "Decentralized nonlinear control of redundant upper limb exoskeleton with natural adaptation law," in *2022 IEEE-RAS 21st International Conference on Humanoid Robots (Humanoids)*. IEEE, 2022, pp. 269–276.
- [55] S. Mirić, R. Giuffrida, D. Bortis, and J. W. Kolar, "Dynamic electromechanical model and position controller design of a new high-precision self-bearing linear actuator," *IEEE Transactions on Industrial Electronics*, vol. 68, no. 1, pp. 744–755, 2020.
- [56] L. Romeral, J. C. Urresty, J.-R. Riba Ruiz, and A. Garcia Espinosa, "Modeling of surface-mounted permanent magnet synchronous motors with stator winding interturn faults," *IEEE Transactions on Industrial Electronics*, vol. 58, no. 5, pp. 1576–1585, 2011.
- [57] X. Wang, Z. Wang, Z. Xu, M. Cheng, and Y. Hu, "Optimization of torque tracking performance for direct-torque-controlled pmsm drives with composite torque regulator," *IEEE Transactions on Industrial Electronics*, vol. 67, no. 12, pp. 10 095–10 108, 2020.
- [58] Y. Hao, L. Quan, S. Qiao, X. Lianpeng, and X. Wang, "Coordinated control and characteristics of an integrated hydraulic–electric hybrid linear drive system," *IEEE/ASME Transactions on Mechatronics*, vol. 27, no. 2, pp. 1138–1149, 2021.
- [59] A. Vesterinen, G. R. Petrovic, and J. Mattila, "Elastodynamic performance evaluation and comparison in hydraulic and electromechanical linear actuator driven heavy-duty manipulators," in *Global Fluid Power Society Ph. D. Symposium*. River Publishers, 2024, pp. 1–21.
- [60] C. Lai, G. Feng, J. Tian, Z. Li, Y. Zuo, A. Balamurali, and N. C. Kar, "Pmsm drive system efficiency optimization using a modified gradient descent algorithm with discretized search space," *IEEE Transactions on Transportation Electrification*, vol. 6, no. 3, pp. 1104–1114, 2020.
- [61] A. Balamurali, G. Feng, C. Lai, J. Tjong, and N. C. Kar, "Maximum efficiency control of pmsm drives considering system losses using gradient descent algorithm based on dc power measurement," *IEEE Transactions on Energy Conversion*, vol. 33, no. 4, pp. 2240–2249, 2018.
- [62] M. Tahkola, J. Keränen, D. Sedov, M. F. Far, and J. Kortelainen, "Surrogate modeling of electrical machine torque using artificial neural networks," *IEEE Access*, vol. 8, pp. 220 027–220 045, 2020.

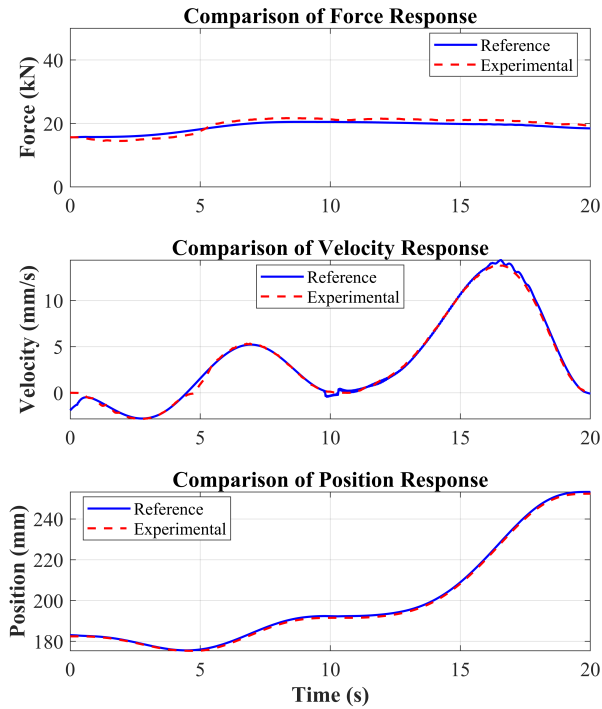


Fig. 15. Experimental tracking results for the tilt actuator with planar triangular trajectory, illustrating performance under 2D constrained motion.

- [63] L. Sciavicco and B. Siciliano, *Modelling and control of robot manipulators*. Springer Science & Business Media, 2001.
- [64] M. Alzayed and H. Chaoui, "Efficient simplified current sensorless dynamic direct voltage mtpa of interior pmsm for electric vehicles operation," *IEEE Transactions on Vehicular Technology*, vol. 71, no. 12, pp. 12 701–12 710, 2022.
- [65] A. Varatharajan, G. Pellegrino, and E. Armando, "Direct flux vector control of synchronous motor drives: Accurate decoupled control with online adaptive maximum torque per ampere and maximum torque per volts evaluation," *IEEE Transactions on Industrial Electronics*, vol. 69, no. 2, pp. 1235–1243, 2022.
- [66] M. Heydari Shahna, M. Bahari, and J. Mattila, "Robustness-guaranteed observer-based control strategy with modularity for cleantech emla-driven heavy-duty robotic manipulator," *IEEE Transactions on Automation Science and Engineering*, vol. 22, pp. 10 248–10 273, 2025.
- [67] M. Bahari, A. Paz, M. H. Shahna, P. Mustalahti, and J. Mattila, "System-level efficient performance of emla-driven heavy-duty manipulators via bilevel optimization framework with a leader-follower scenario," *IEEE Transactions on Automation Science and Engineering*, pp. 1–1, 2025.
- [68] M. Heydari Shahna, M. Bahari, and J. Mattila, "Robust decomposed system control for an electro-mechanical linear actuator mechanism under input constraints," *International Journal of Robust and Nonlinear Control*, vol. 34, no. 7, pp. 4440–4470, 2024.